Anisotropic Plasmonic CuS Nanocrystals as a Natural Electronic Material with Hyperbolic Optical Dispersion

R. Margoth Córdova-Castro[‡], Marianna Casavola[‡], Mark van Schilfgaarde, Alexey V. Krasavin, Mark Green, David Richards, and Anatoly V. Zayats*

Department of Physics and London Centre for Nanotechnology, King's College London, London WC2R 2LS, United Kingdom

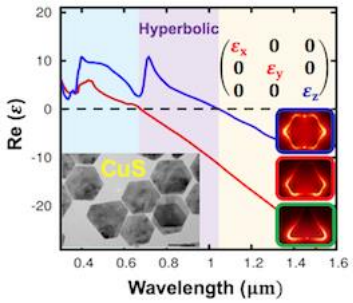

ABSTRACT. Copper sulfide nanocrystals have recently been studied due to their metal-like behavior and strong plasmonic response, which make them an attractive material for nanophotonic applications in the near-infrared spectral range, however, the nature of the plasmonic response remained unclear. We have performed a combined experimental and theoretical study of the optical properties of copper sulfide colloidal nanocrystals and show that bulk CuS resembles a heavily doped p-type semiconductor with a very anisotropic energy band structure. As a consequence, CuS nanoparticles possess key properties of relevance to nanophotonics applications: they exhibit anisotropic plasmonic behavior in the infrared and support optical modes with hyperbolic dispersion in the 670-1050 nm spectral range. We also predict that the Ohmic loss is low compared to conventional plasmonic materials such as noble metals. The plasmonic

resonances can be tuned by controlling the size and shape of the nanocrystals, providing a playground for future nanophotonic applications in the near-infrared.

KEYWORDS: plasmonics, colloidal nanocrystals, hyperbolic dispersion, localized surface plasmons

The electromagnetic response of materials is defined by their dielectric permittivity. In metals, the real part of the permittivity is negative below the plasma frequency because of the polarization response of free electrons, which makes them good reflectors. When it is positive, as it is in dielectric and semiconductor materials, the medium supports propagating electromagnetic waves. If an anisotropic material has 'metallic' permittivity for one polarization and 'dielectric' for another, the electromagnetic dispersion has hyperbolic isofrequency surfaces and is often called 'hyperbolic'.[1-4] This property means that hyperbolic materials may also exhibit the so-called epsilon-near-zero behavior in the spectral range when the negative component of the permittivity tensor crosses zero (at the plasma frequency).[4-6] Such anisotropic materials can be found in nature in the far-infrared spectral range where these optical properties are governed by phonon-polariton contributions.[7-9] In the near-infrared and visible spectral ranges, hyperbolic optical dispersion can be achieved with metamaterials, based on plasmonic-dielectric multilayers, plasmonic nanorod arrays or resonant semiconductor heterostructures.[1-4] Hyperbolic metamaterials have demonstrated numerous unusual properties associated with the nature of the supported modes, such as negative refraction, enhanced refractive index sensitivity and nonlinear optical properties, as well as a strong Purcell effect for the control of spontaneous emission.[1-10] However, natural materials with hyperbolic optical dispersion are sparce in the visible spectral range.

On the other hand, the optical response of plasmonic nanoparticles is significantly restricted by the range of available plasmonic materials and particularly their losses.[9-13] The optical response of a plasmonic nanoparticle is determined by the localized surface plasmon (LSP) modes it supports, and is of utmost importance for sensing, imaging and nonlinear optical applications. Dielectric coatings and shape effects help to alleviate material restrictions on the LSP wavelength[12,13] and hyperbolic metaparticles have recently been demonstrated as a zero-dimensional realization of a hyperbolic metamaterial with a rich and tuneable spectrum of the plasmonic resonances.[14] However, Ohmic losses in traditional materials remain a critical issue. The search for alternative plasmonic materials have recently resulted in a plethora of plasmonic media with different plasma frequencies and losses based on oxide and nitride compounds and semiconductor nanoparticles.[7-9]

Copper chalcogenides have attracted interest in nonlinear photonics and plasmonics for their ability to sustain several levels of doping, as different metastable phases give rise to a distinctive plasmonic response.[27] In colloidal synthesis routes, the stoichiometry and chalcogen composition can be tuned by modulating the Cu and chalcogen precursor ratio in solution, or post-synthesis, by reversible redox reactions, ultimately producing tuneable LSP resonances in the near and mid IR.[24-28] Amongst different copper chalcogenide combinations, stoichiometric CuS is a particularly attractive plasmonic material for its exceptionally high carrier density, ease of preparation, low toxicity and high stability.[16-18] In contrast, while $Cu_{2-x}S$[15] (and similar chalcogenides such as $Cu_{2-x}Se$ and $Cu_{2-x}Te$) can sustain different amounts of doping and be metastable in several crystallographic structures (for different x) and are also relatively easy to convert from one to another by performing redox reactions, they can also change over time simply by oxidation in air. With the development of methods to grow CuS nanocrystals (NCs) with a

strong plasmonic response in the near-infrared, several applications have been proposed in biomedicine, photovoltaics, chemical sensing, and electronics.[16-39]

Stoichiometric copper sulfide in the covellite phase, CuS, adopts a complex hexagonal crystal structure in bulk.[35] Despite significant advances in achieving complex structures with tuneable characteristics, the intrinsic properties of CuS, such as the band structure and the nature of plasmonic resonances, are still not well understood. In order to describe the optical properties of CuS nanocrystals, the approaches to model the LSP resonances and their dependence on size and refractive index of surroundings have mostly relied on the use of the scattering theory in the quasi-static limit within the framework of the Drude-Sommerfeld model of the isotropic electron gas.[17,27,32] While such an approach is reasonably adequate for metal particles, it has to be taken with due reservation when applied to doped semiconductors with an anisotropic crystal lattice. Some of the features of the plasmonic spectra have been reproduced in specific cases with a simple Drude model using multiple fitting parameters, but its applicability to an anisotropic material is difficult to justify.

In this paper, we show that CuS has the optical properties of a natural hyperbolic material in the 670–1050 nm spectral range and an anisotropic plasmonic material at the longer wavelengths, where its optical losses are lower than in noble metals. To this end, *ab-initio* calculations within the quasiparticle self-consistent *GW* approximation[40,41] (QS*GW*, where *GW* is the single particle Green's function *G* with the screened Coulomb interaction *W*) were performed to determine the electronic band structure of CuS and the macroscopic dielectric function. QS*GW* is perhaps the most universally applicable, true *ab initio* theory for electronic states in extended systems that exists today. It has a proven ability to consistently and reliably predict quasiparticle levels for a wide range of materials, e.g. graphene,[42] Fe-based superconductors,[43] pyrite,[44] and

$NH_3CH_3PbI_3$,[45] in a consistent and parameter-free manner that cannot be achieved by other theories. The QS*GW*-calculated electronic band structure and permittivity reveals the existence of the hyperbolic optical properties of CuS in the visible and anisotropic plasmonic response in the near-infrared spectral range. These properties have been confirmed by studying the experimental optical response of CuS nanocrystals with different geometries (shape and aspect ratio) and refractive index dependencies. The experimentally observed LSP resonances and their size and refractive index dependences have been reproduced in the simulations without any fitting parameters. The observed optical properties of CuS, with Ohmic losses lower than typical plasmonic metals such as Au and Ag, are important for typical application of hyperbolic and plasmonic materials in sensing, nonlinear optical devices, Purcell factor enhancement and hot-carrier generation in the visible and near-infrared spectral ranges.

RESULTS AND DISCUSSION

Electronic Band structure from *ab initio* calculations.

The electronic band structure of CuS in the ideal covellite phase was calculated within the QS*GW* approximation (Figure 1, see details of the calculations in Methods), from which CuS may be considered to be a heavily doped p-type semiconductor with a direct gap calculated to be 0.36 eV at the Γ point. The alternative local density approximation (LDA) predicts the gap to be negative, in line with the LDA tendency to underestimate bandgaps. In the QS*GW* band structure the valence band maximum (VBM) and the Fermi level (E_F) are separated by 0.93 eV, with the states between E_F and the valence band maximum containing two electrons: therefore, stoichiometric CuS is hole-doped by 1/3 electron per (Cu,S) pair, leading to the free-carrier concentration of 2.9×10^{21} cm^{-3}.

This makes an interesting contrast to stoichiometric Cu_2S, which forms in the chalcocite structure and is thought to be a narrow-gap insulator.[50]

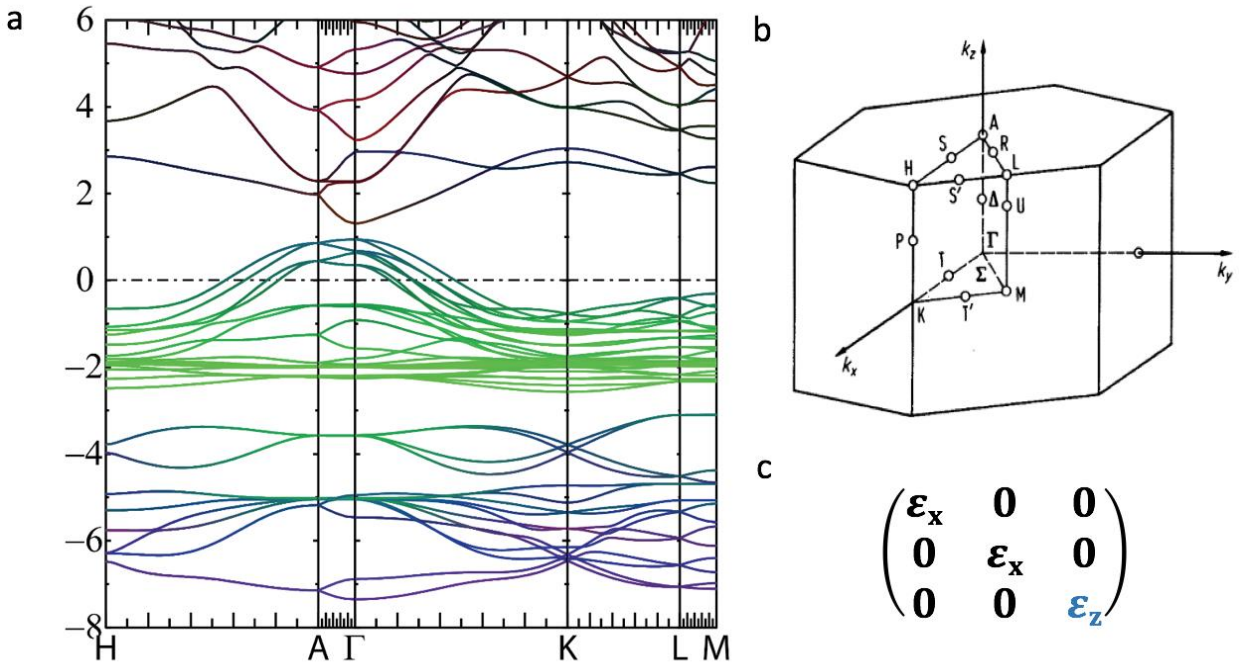

Figure 1. (a) Electron band structure of covellite CuS calculated in the QS*GW* approximation. Fermi level is set to 0. Colours depict the orbital character: red, green, and blue indicate projections onto Cu *s* + S *s*, Cu *d*, and S *p* states, respectively. All other orbitals are black. (b) CuS crystal structure in the reciprocal space. (c) Permittivity tensor components of CuS.

As can be seen by inspecting the colour weighting of the bands, the Cu *d*-bands are centred at $E_F = -2$ eV, they hybridize with the S *p*-states. Thus, the valence bands between E_F and the VBM consist of an approximately equal mix of S *p*- and Cu *d*-orbitals. The conduction band consists of a mixture mostly of Cu+S *s*-states. If the band structure is calculated at the Perdew-Burke-Ernzerhof (PBE) equilibrium crystallographic geometry instead of the experimentally measured one[18] used in Fig. 1, the gap changes by only -0.02 eV, which is smaller than the precision to which

QS*GW* can predict the gap. QS*GW* tends to slightly overestimate gaps, so we can expect that the true gap of stoichiometric CuS is close to, but slightly smaller than 0.36 eV.

Dielectric function calculation.

The longitudinal part of the dielectric function was calculated within the random phase approximation (RPA), starting from the QS*GW* Hamiltonian, as

$$\varepsilon(\omega) = \left[\lim_{q\to 0} \varepsilon^{-1}_{G=G'=0}(q,\omega)\right]^{-1}, \quad (1)$$

both with and without local fields (neglecting the off-diagonal G components of ε). The RPA can be extended by including ladder diagrams, as was done for Cu_2O.[51] However, because the system is metallic, the effects of ladders are expected to be relatively small. The anisotropic dielectric function calculated in the 0.5-7 eV range shows that the effect of local fields is relatively modest (Figure S1). Nevertheless, in the following, a more precise permittivity is used, that has been obtained with local field corrections included (Figure 2 and S1).

The real part of each permittivity component is negative at low frequencies, increasing with ω and passing through zero at a corresponding plasma frequency, which is characteristic of a metallic material with significant free carrier concentration (Figure 2a). Clearly, there is a strong anisotropy, with Re$\{\varepsilon_z\}$ crossing zero at $\hbar\omega_{pz}$=1.18 eV (1047 nm), while Re$\{\varepsilon_x\}$ present a higher plasma frequency at $\hbar\omega_{px}$=1.84 eV (673 nm) (Figures 2 and S1). By symmetry, $\varepsilon_x = \varepsilon_y$ so the permittivity tensor has only two independent elements $\varepsilon_x(\omega)$ and $\varepsilon_z(\omega)$. Note also these

components tend to approach zero near 5 eV (Figure S1). Between ω_{px} and ω_{pz} the real parts of $\varepsilon_x(\omega)$ and $\varepsilon_z(\omega)$ have opposite signs. In this region, then, CuS behaves as a bulk material with naturally occurring hyperbolic dispersion of optical modes. This structure of the permittivity tensor (Figure 1c) with two negative and one positive components corresponds to Type 1 hyperbolic dispersion, characteristic, *e.g.*, for layered plasmonic/dielectric multilayers.[1,3,4] The imaginary parts of ε_x and ε_z show that CuS has lower losses than conventional plasmonic metals in the NIR spectral range (Figure 2b). Figure 2(c-e) and Figure S2 show the isofrequency contours of the electromagnetic waves in bulk CuS at selected wavelengths in the elliptic (anisotropic dielectric), hyperbolic and anisotropic plasmonic dispersion regions. The curves for the real components reflect the wavelength of the supported modes, while the imaginary components represent the mode attenuation in different propagation directions. The evolution of the dispersion from the elliptical to hyperbolic regime is seen as a drastic change in the isofreqeuncy curves and the appearance of the modes with large wavevectors in the latter case. The ideal hyperbola and very large wavevectors are however truncated due to the presence of the losses. It is important to note that because of this, the supported wavelengths are large enough compared to the size of the studied nanostructures even in the hyperbolic dispersion regime so that the modelling of the nanoparticle resonances can be performed in the electrostatic approximation. There is also a clear difference in the propagation loss of the modes propagating mostly in *z*- direction with the modes propagating mostly in *x* (and *y*) -directions in the hyperbolic regime. Conventional dichroism of the uni-axial dielectric is observed in the elliptic regime. Finally, at longer wavelengths, for which plasmonic behavior is observed, modes do not propagate in any direction (Figure 2e).

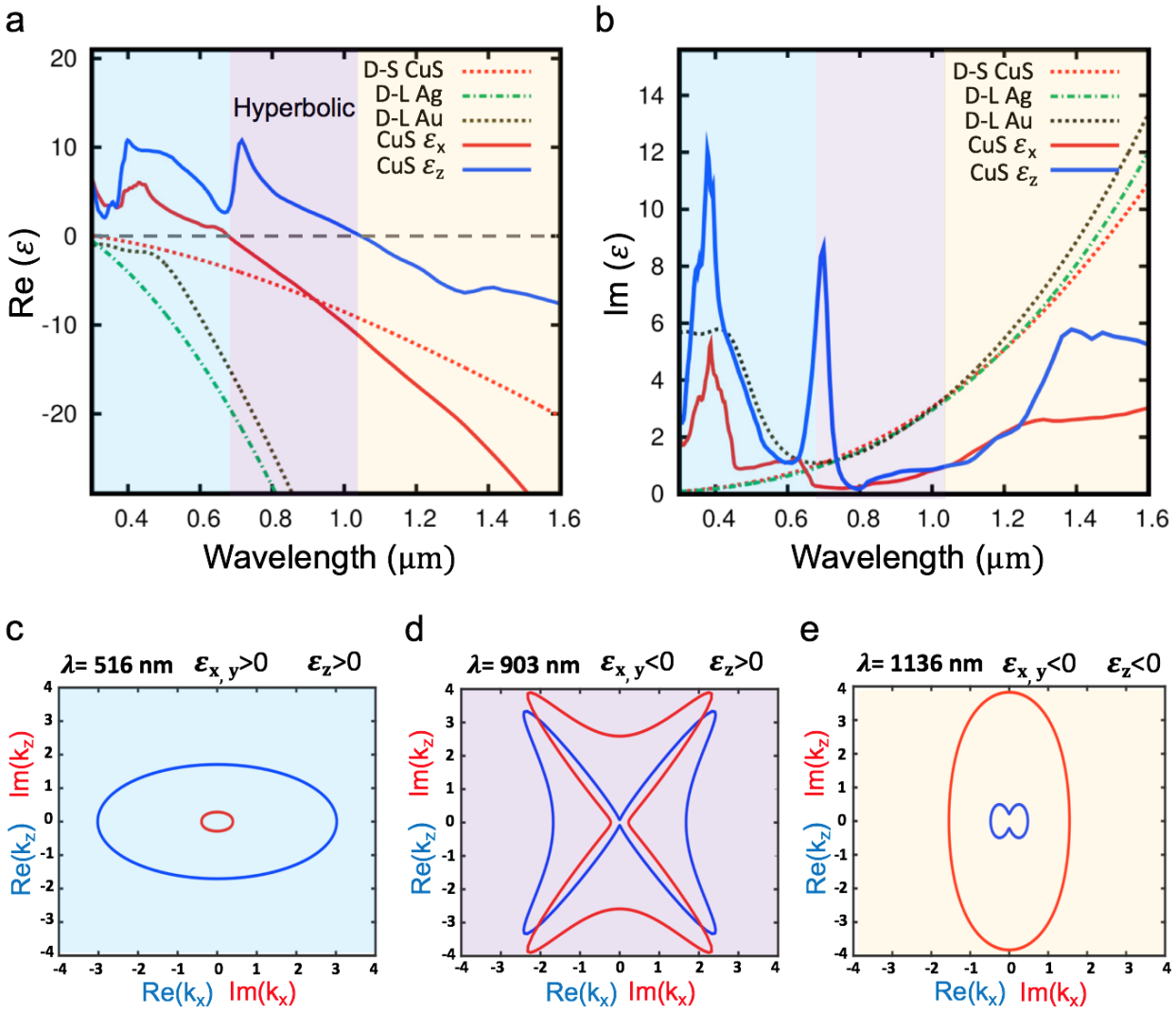

Figure 2. Real (a) and imaginary (b) parts of the permittivity calculated for CuS within the QS*GW*-RPA approximation. The shading marks the dielectric, hyperbolic, and plasmonic optical dispersion regimes. For comparison, the permittivities of Au and Ag, taken from the Drude-Lorenz fit,[50] and CuS, estimated by fitting the experimental LSP resonances using the Drude-Sommerfeld method (see Supplementary Information), are also plotted (indicated by D in the legend). (c-e) Isofrequency curves for (blue) [Re{$k_x(\omega)$}, Re{$k_y(\omega)$}=0, Re{$k_z(\omega)$}], refractive index related, and (red) [Im{$k_x(\omega)$}, Im{$k_y(\omega)$}=0, Im{$k_z(\omega)$}], absorption related, parts of the wavevector wavevector for the TM electromagnetic waves with the electric field component in z-direction in

bulk anisotropic CuS for the vacuum wavelengths $\lambda = 2\pi/\omega$ in different dispersion regimes: (c) elliptic (anisotropic dielectric), (d) hyperbolic and (e) anisotropic plasmonic.

Optical properties of CuS nanocrystals.

CuS colloidal nanocrystals were synthesized by the hot injection of a sulfur precursor in oleylamine into a solution of copper (I) chloride, oleylamine, oleic acid, and octadecene under inert atmosphere (see Methods for the details of the synthesis).[17,23-26] Due to the intrinsic hexagonal crystallographic structure of covellite, the NCs had a tendency to grow with a platelet-like morphology and a mixture of shapes, either hexagonal, triangular, or circular; the preferential growth in the longitudinal direction of hexagonal covellite is possibly explained by the combination of kinetically-driven conditions and in light of the preferential absorption of surfactants on the (001) crystallographic facets. Figure 3 shows the example of the TEM micrographs of NCs with thicknesses in the 5 ± 0.5 nm range and increasing aspect ratio (see Methods and Figures S3 and S4 for the details of the structural characterization). NCs with a lateral size of 16, 19 and 24 nm were synthesized by changing the concentration and ratio of surfactants, while lower temperatures allowed for the formation of platelets in the 50-200 nm lateral size range.

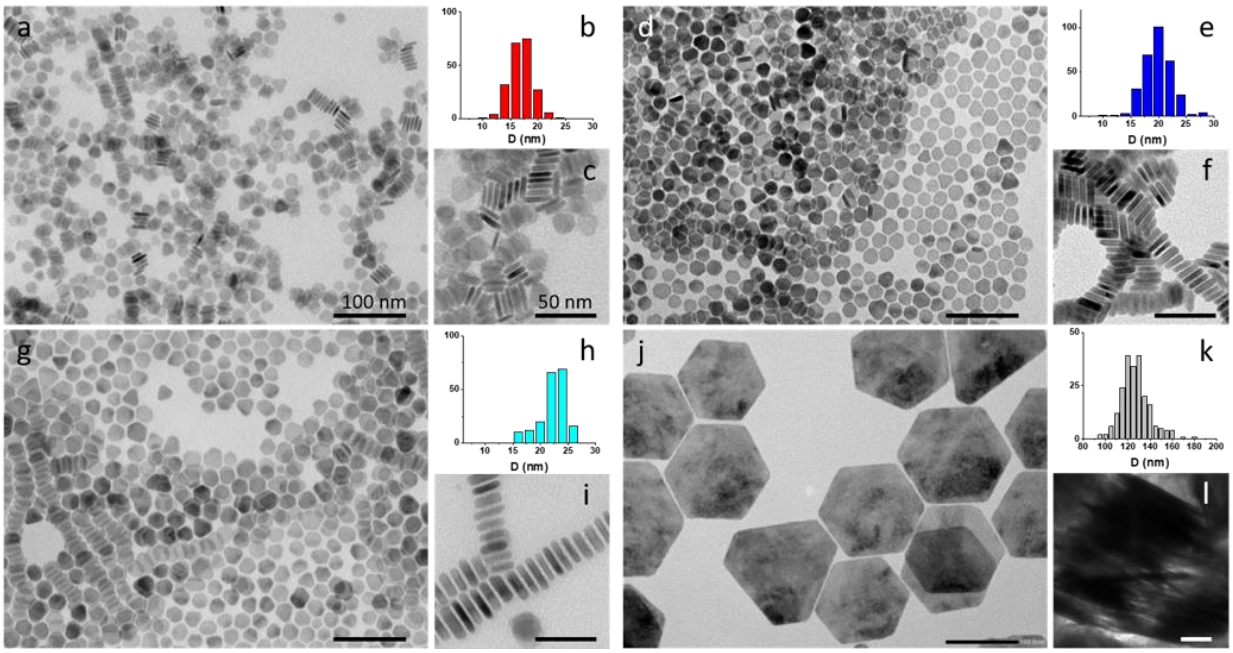

Figure 3. TEM micrographs of CuS NCs with a similar thickness of 5 ± 0.5 nm and a lateral size of (a,c) 16 ± 3 nm, (d,f) 19 ± 3 nm, (g,i) 24 ± 3 nm, and (j,l) 127 ± 10 nm. The NC size is defined as a diameter of a circle circumscribed around the NC shape. The scale bar is 100 nm for (a,d,g,j) and 50 nm for (c,f,i,l). (b,e,h,k) The size distribution histograms for samples (a,d,g,j) were obtained from several TEM micrographs by measuring the size of 200 NCs.

Using the geometrical parameters found from the TEM images (Figure 3) and the dielectric permittivities from the *ab initio* calculations (Figure 2), the extinction spectra of the NCs have been simulated. Figure 4 shows the calculated spectra of the normalized absorption cross-section for isolated CuS NCs with different shapes with a thickness of 5 nm and a 19 nm lateral size surrounded by a medium with a refractive index of 1.45, illuminated with light having in-plane or out-of-plane polarizations with respect to the NC orientation. Since *x* and *y* in-plane polarization (the wave vector is normal to the NC plane) result in similar curves, only the *x*-polarized case is plotted. For these nanoparticle dimensions, significantly below the wavelength of light, the

extinction is dominated by absorption while scattering is almost zero, such that only absorption cross-sections are shown. Figure 4a shows that the main peaks in the absorption for the in-plane polarization appear below the bulk plasma frequency (approximately 670 nm) and are in the NIR spectral range, where NCs behave as anisotropic plasmonic nanoparticles, supporting LSPs. For comparison, the extinction of an spheroidal nanoparticle of the same dimensions is shown. One can see that the LSP is progressively red-shifted for different shapes, with the spheroidal particle showing the resonance at 1085 nm, the circular NC at 1111 nm, and hexagonal NC at 1136 nm. A lower symmetry NCs exhibit a richer spectrum with two LSP modes, with a triangular NC having most strongly separted modes: one LSP at 943 nm (in the hyperbolic spectral range) and a dominant mode at 1346 nm, which is strongly red-shifted compared to the other shapes.

For the out-of plane polarization (the wave vector is along the NC plane), the bulk plasma frequency corresponds to a wavelength of 1050 nm. The spectra in this case overlap for all the shapes of the NCs, apart from the reference spheroidal shape with three main peaks observed at around 328 nm, 665 nm and 1077 nm wavelengths (Figure 4b). The first two peaks in the absorption spectra originate from material losses due to interband transitions (cf. Figure 2b) where CuS does not have plasmonic behavior. The observed absorption is dominant for CuS nanocrystals for the in-plane light polarization for the studied range of NC dimensions, which is in agreement with previous studies.[17,26,27] Interestingly, for both in- and out-plane directions, the imaginary part of the permittivity is lower than in the convetional plasmonic materials in the wavelength range where CuS has metallic behavior and where the LSP peaks are situated.

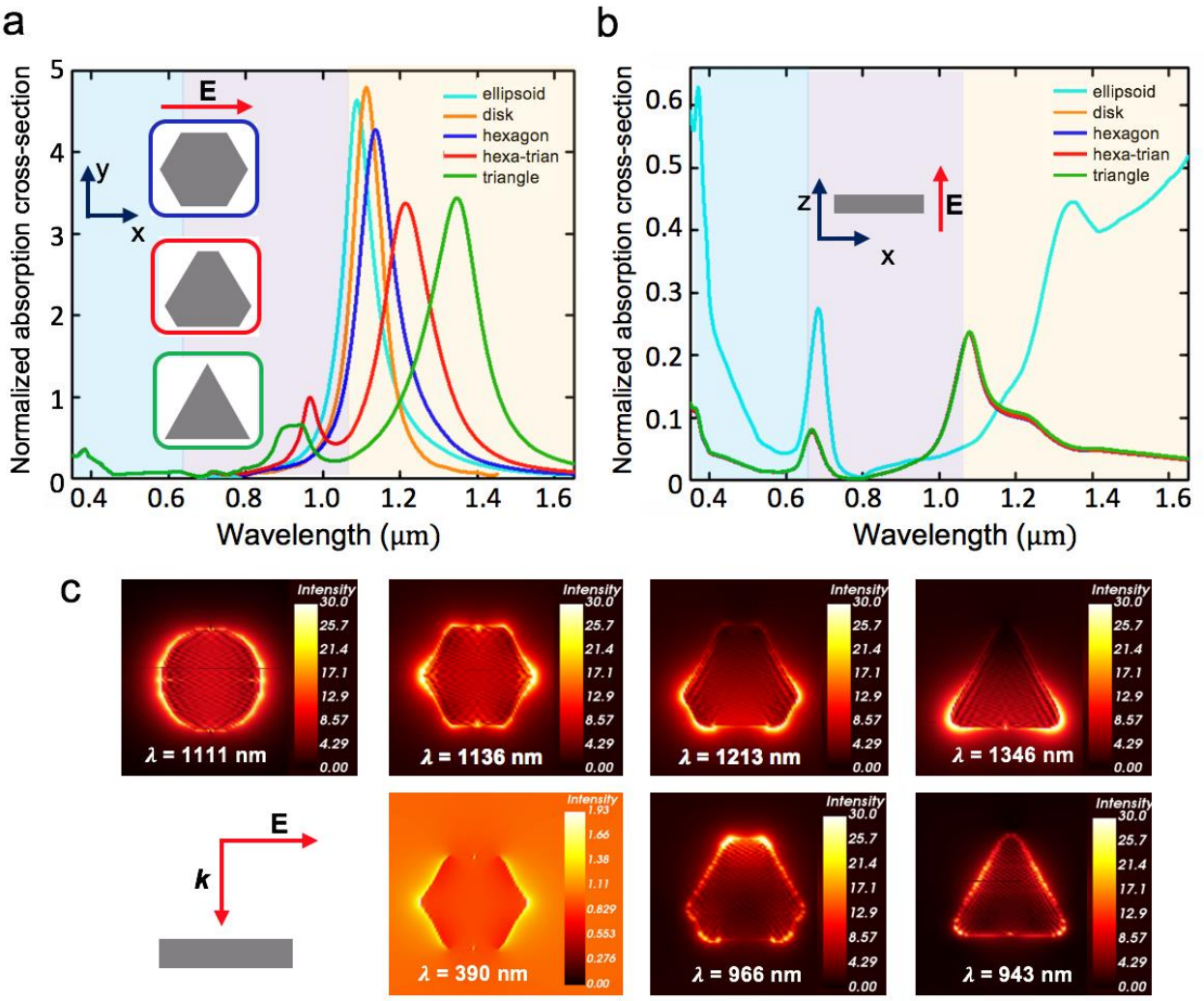

Figure 4. (a-b) Calculated spectral dependences of a normalized absorption cross-section for isolated CuS NCs of a 19 nm lateral size and a 5 nm thickness with various shapes (circular, hexagonal, hexa-triangular and triangular plates and an oblate spheroid) surrounded by a medium with a refractive index of 1.45, upon illumination with a plane wave along the crystal axes for (a) in-plane polarization (the electric field along *x* axis and the wavevector along *z*-axis) and (b) out-of-plane polarization (the electric field along the *z*-axis with the wavevector directed along *x* axis). (c) Near field intensity maps for the CuS NCs with various shapes calculated at the resonant conditions for in-plane illumination. The schematic of the illumination is also shown.

For the plasmonic modes, relatively high field enhancement (up to 50) is observed in the near-field distributions at the resonant frequencies (Figure 4c). Considering the shape effects in triangular and hexagonal NCs, where the in-plane orientation of the incident electric field is important, the absorption spectra and near-field calculations for in-plane polarization along the *y*-axis are presented in Figure S5 for the same system as in Figure 4. The normalized absorption cross-section for the triangular NC (Figure S5a) has two resonant peaks at the same frequencies as for *x* polarization but the peak for the mode at 943 nm is higher for the *y*-polarization, while the peak for the mode at 1346 nm is higher for *x*-polarization. For the hexagonal NC (Figure S5b), the spectral curves match for both in-plane directions as a result of the higher order of the sparial symmetry of hexagonals NCs (compared to those with a triangular shape). Figure S6 shows the near-field intensity maps for the out-of-plane polarization for the hexagonal shape, as for this polarization all the other shapes present similar behavior in the near-field region. The peaks around 328 nm and 665 nm occur above the plasma frequency and clearly have a non-plasmonic origin. For the LSP peak around 1077 nm, a very intense local field across the entire particle is observed.

The experimentally studied CuS NCs were in a colloidal form in a solvent, i. e. the NCs are randomly oriented; therefore, an averaged optical response from the two orientations with respect to the light polarization will be observed, additionally averaged over a variety of shapes present in the solution. The measured extinction spectra exhibit a dominant resonance in the near-infrared spectral range, where CuS has plasmonic behavior, with the indication of an additional resonance at, or below 400 nm, the short-wavelength cut-off of the spectrometer (Figure 5). The position of the former resonance depends on the refractive index of the surroundings, which is a characteristic of a localized surface plasmon, while the spectral form of the latter short-wavelength

feature is independent of surroundings and, hence, is related to intrinsic absorption of CuS. The measured dependences indicate an average sensitivity ($S=\Delta\lambda/\Delta n$) to refractive index variations of $S \approx 330$ nm/RIU.

To simulate the effect of the surrounding medium and the nanoparticle size on the LSP resonance, the prevailing hexagonal shape of the NCs (Figure 3) was initially considered: the numerical spectra correctly reproduce the position, the LSP resonance shift and LSP absorption strength for different refractive indices also correctly predicting the short-wavelength absorption resonance, related to interband transitions, without any fitting parameters. The absorption cross section obtained by averaging of the possible NC orientations shows a progressive red-shift of the LSP resonance with a refractive index sensitivity $S \approx 250$ nm/RIU, which is in a good agreement with the experimental data (Figure 5b). The sensitivity is also in agreement with other reports ($S \approx 350$ nm/RIU).[27] At the same time, the spectral broadening of the experimental peaks, compared with the numerical simulations, can be attributed to the size and shape distribution in the measured colloidal NCs. The consideration of other shapes of the same size present in the solution leads to the broadening of the dominant absorption line of the hexagonal crystals in both short and long wavelength sides (Figure S8), so that the resulting resonance aquaries the width FWHM ≈ 310 nm, compared to FWHM ≈ 115 nm for only hexagonal shape, in the case of surrondings with a refractive index n=1.45. The distribution in the NC sizes leads to additional broadening (Figure 6), resulting in FWHM ≈ 335 nm for the 6 nm average size distribution. This compares well with the resonance width observed in the experiment (FWHM ≈ 410 nm (Figure 5a)), where stronger size deviations may contribute to additional broadening. Interestingly, the shape of the resonant peak is determined by the LSPs of NCs of lower symmetry shapes for both long wavelength and short wavelength sides from the dominant LSP of the hexagonal NCs. The contribution of a short-wavelength shoulder which is related to the LSPs for the light polarization normal to the NC plane increases for higher refractive indices of surroundings (Figure S8). Thus, the shift of the maximum in the extinction with the refractive index is determined by the shift of the LSP of dominant hexagonal NCs, while the width of the resonance is determined by the presence of other shapes and NC size distribution.

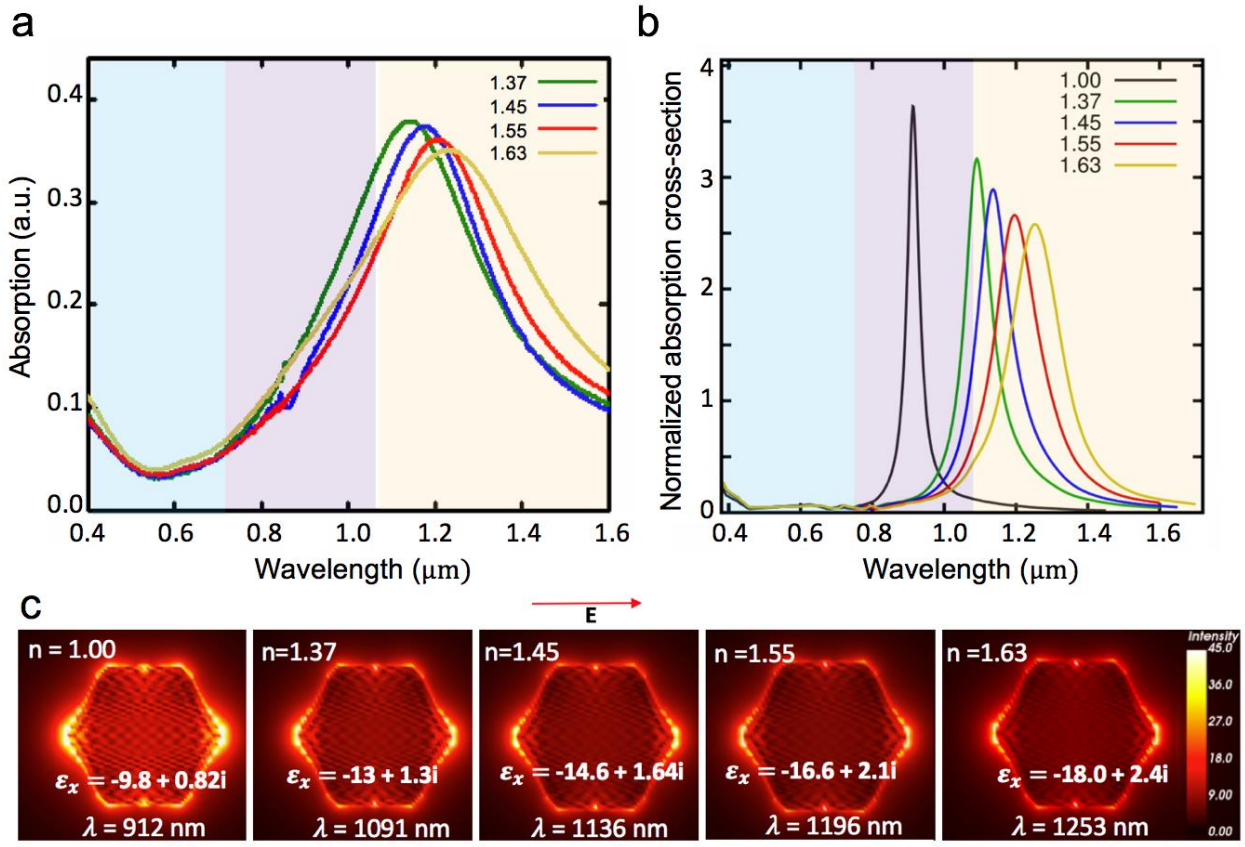

Figure 5. (a) Experimental absorption spectra of CuS NCs and (b) calculated normalized absorption cross-section for isolated CuS NCs (19 nm lateral size and 5 nm thickness), dispersed in solvents with various refractive indices: hexane (1.37), chloroform (1.45), ortho-dichloro benzene (1.55), and CS_2 (1.63). In (a), the extinction measured in CS_2 solvent was normalized to the same concentration as for the other solvents. (c) Near field intensity maps for a hexagonal isolated NC at the resonant condition for the in-plane polarized illumination.

With the increase of the refractive index of the surrounding medium, the width of the calculated CuS NC absorption peak increases and the maximum decreases (Figure 5b), while the field enhancement increases (Figure 5c). Figure S7 shows the calculated absorption spectra for different light polarizations, corresponding to the averaged spectra in Figure 5b. In the case of the

in-plane polarized illumination, the spectral red shift is higher than in the case of the out-plane polarized illumination. The maximum of the absorption peak increases with the increase of the surrounding medium refractive index in the case of the out-plane polarized illumination, with the opposite behavior in the case of the in-plane polarized illumination. It is interesting to note that the simulated spectra for the nanocrystals in air (n=1) exhibit the LSP resonance at 912 nm, in the spectral region where CuS has a natural hyperbolic dispersion, and the plasmonic resonance comes only from the NCs oriented along the in-plane direction with respect to the linearly polarized incident beam (this resonance has also the dominant response for longer wavelengths (Figure 5 a,b). A comparison of the refractive index sensitivity of the LSP of CuS NCs to nanoparticles of the same size and shape of Au, in the visible spectral range (325 nm/RIU), and AZO and ITO, in the near infrared (232 nm/RIU), identifies CuS NCs as a good alternative for sensing with the advantages of easy fabrication and nontoxicity (Figure S9). At the same time, the sensitivity of CuS NCs surpasses the sensitivity of standard spherical and nanorod Au nanoparticles,[53] while CuS provides advantages of hyperbolic media in sensing.[54]

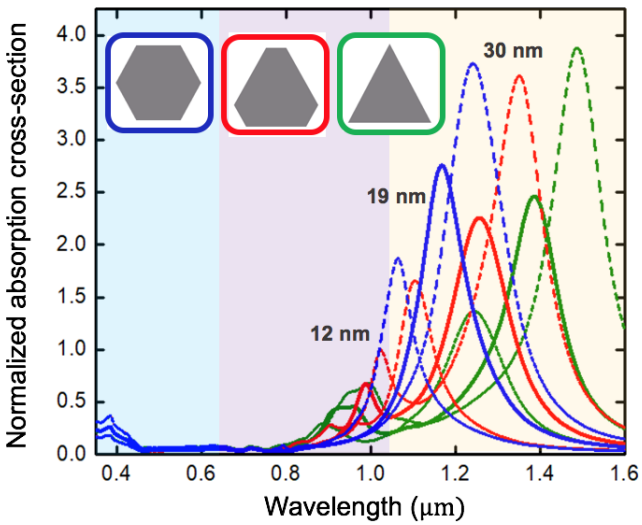

Figure 6. Calculated spectra of normalized absorption cross-sections for CuS nanocrystals of a hexagonal, triangular and hexa-triangular shapes for different lateral sizes: (dash line) 12 nm, (solid line) 19 nm and (dash-dot line) 30 nm. The thickness is 5 nm and the surrounding medium n= 1.45 in all cases. The illumination is linearly polarized with the electric field in a NC plane. The spectra are averaged over random NC orientations with respect to the linearly polarised incident light.

The measured extinction spectra of CuS NCs colloidal solutions having different sizes and the same NC concentration show a progressive shift of the LSP resonance towards higher wavelengths with increasing NC aspect ratio (Figure 7). This behavior is in good agreement with the calculations, also showing that the increase of the NC lateral size from 12 to 24 nm produces a strong increase of the LSP absorption. Experimentally, NCs with higher aspect ratios also showed stronger broadening of the absorption peaks due to the averaging over larger range of different shapes and sizes (Figure 6) of the colloidal NCs for these samples which are less controlled. The calculated absorption at the LSP resonance and the field enhancement also increase with the increase of the NC lateral size; the mode character does not depend on the size in this range (Figure 7c). In all studied cases, the LSP resonances of anisotropic CuS nanocrystals may occur for both orientations of light polarization with respect to the crystal axis; however the dominant LSP modes are mostly defined by the in-plane charge oscillations due to the flat geometry (NCs with sizes up to 100 nm still had a thickness around 5 nm), determined by the nature of the CuS nanocrystal growth.

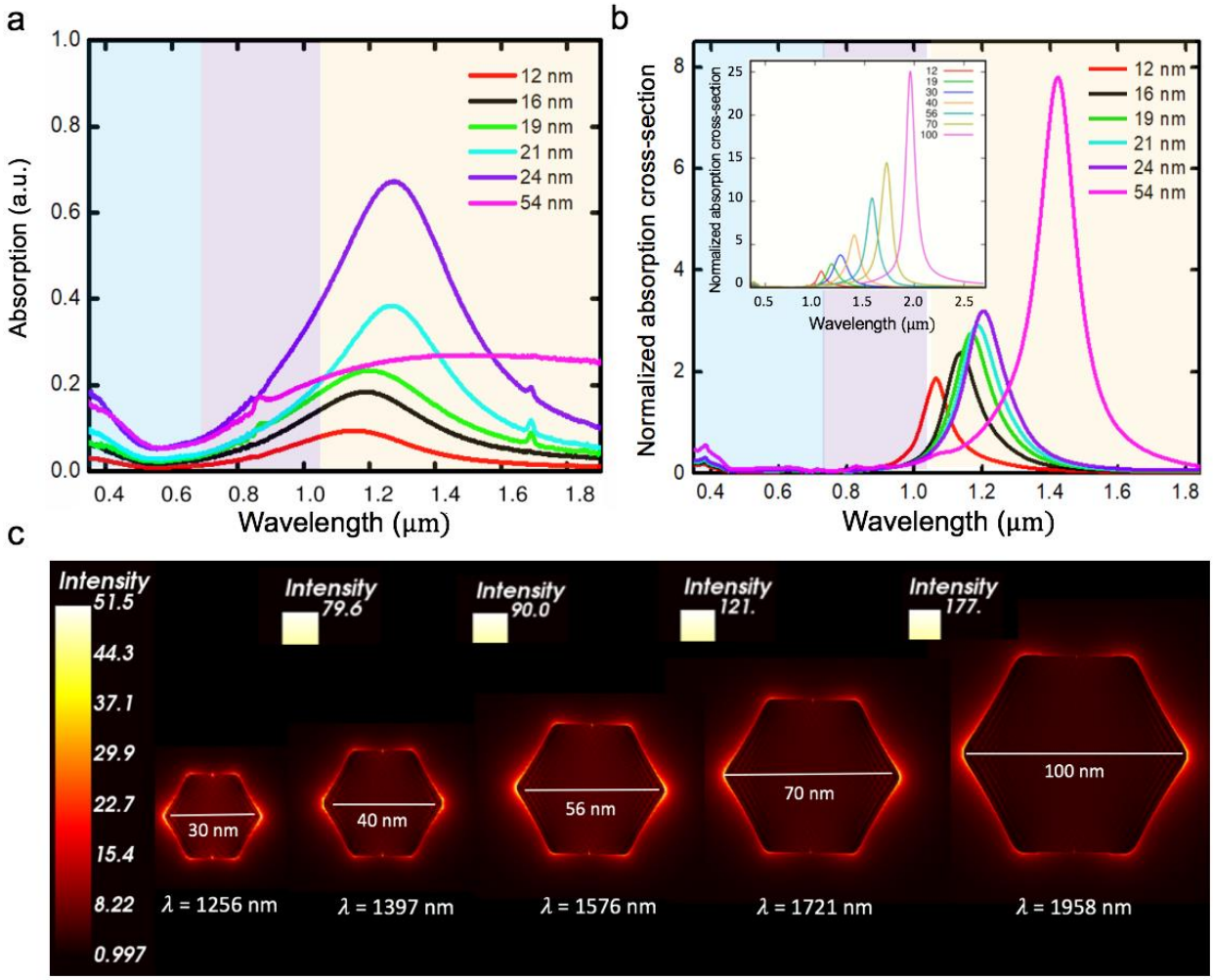

Figure 7. (a) Experimental absorption spectra of the NCs dispersed in tetrachloroethylene (n=1.505) with the average size (determined from TEM) increasing from 12 to 24 nm. (b) Calculated normalized absorption cross-section averaged over the orientation of the hexagonal nanoparticles with respect to light polarization, with the lateral size increasing from 12 to 56 nm. (c) Calculated near-field intensity maps for the hexagonal NCs surrounded by the medium with a refractive index of 1.505 for various lateral sizes and a 5 nm thickness at the LSP resonant conditions.

It is interesting to compare the spectral dependencies observed and simulated above to the prior empirical models used to evaluate the properties of LSP in CuS nanocrystals (See Supplementary Materials).[17,27-31] By solving the inverse problem which takes the experimental values of the position and the linewidth of the measured absorption peak as the input parameters, the Drude-Sommerfeld model can be used to determine an isotropic permittivity of CuS, using the plasma frequency and damping as fitting parameters, as is explained in detail in Methods (Figure 2a,b). This approach has been followed in all the previous works[17,22-32] on the evaluation of plasmonic behavior of CuS and Cu_2S. Although the calculated extinction spectra correlate well with the experimental absorption curves upon fitting (Figure S10), this method has limitations due to important restrictions made by imposing the resonant and damping values taken from the experimental curves, and fails in a broad spectral range if fitting parameters are kept fixed. In particular, this model does not describe the measured sensitivity of the CuS LSP on a refractive index of surroundings and NC size. In this approach it is also impossible to distinguish at which energies the material, which is intrinsically a semiconductor, has metallic behavior and the anisotropic and hyperbolic behavior is completely missed. In contrast the present approach fits the bulk RPA dielectric function without free parameters. Owing to the high precision of QS*GW*, the model may be expected to approximate the exact dielectric function of bulk CuS well. Application of the model to nanocrystals is shown to be similarly reliable, allowing us to distinguish plasmonic resonances from pure interband absorption of the material (Figure 2b).

It should be noted that the representation of the anisotropic properties of CuS (Figure 2a,b) might approximated using two Drude-Lorenz models with two different sets of Drude parameters for two optical directions and with appropriate set of Lorenz oscillators in each case. To implement such a Drude-Lorentz representation for each optical axis, one would require one Drude model

and at least three Lorenz oscillators, as can estimated from Figure 2a,b (but this might be an underestimation). Thus, altogether 12+ fitting parameters for each optical axis will be required. While different plasma frequencies can be related to different hole masses in different directions, we do not see any plausible way to assign with any certainty the Lorenz oscillators to the particular transitions in the band structure in Figure 1 due to its complexity.

Finally, we note that the typical 5 nm thickness of the studied CuS NCs with (001) facets corresponds to a thickness of just 3 covellite unit cells. A such, it is reasonable to expect that quantum confinement of electronic states will occur for carrier motion normal to the discs (along Γ-A, Figure 1). To perform an *ab initio* calculation of the full dielectric response of an isolated CuS NC is not possible at this point, as the QS*GW* implementation requires periodic boundary conditions. Nevertheless, the flat dispersion in Γ-A of the relevant valence band states, both above and below the Fermi level, means that quantum confinement effects are not expected to affect the density of states and optical response of this system at room temperature, such that an assumption of a bulk permittivity is considered to be a good approximation. Quantum confinement is not expected to play a role in the in-plane band dispersions, given the high effective mass of bands at the zone center along Γ-K, a typical lateral size of 20 nm and the fact that the measurements are performed at room temperature.

CONCLUSIONS

In general, CuS belongs to the realm of copper chalcogenides ($Cu_{2-x}E$ with E= S, Se, Te) with well established synthesis methods which allow for the exploitation of plasmonic properties in the near and mid IR, by changing their composition in S, Se, Te, as well as metal-to-chalcogen ratio. These

materials may provide a basis for a database of nanocrystals with tuneable plasmonic resonances for future nanophotonic applications.

We demonstrate that CuS in the covellite phase has two of the most interesting optical properties of relevance to nanophotonic materials, plasmonic behavior and hyperbolic dispersion. Using first principles calculations we reveal that CuS is a natural hyperbolic material in visible spectral range and anisotropic plasmonic material in the infrared. The former underlines the presence of a rich LSP spectrum, with in-plane LSP typically dominating for small particles. With the availability of ordered assemblies of CuS NCs over realtively large areas facilitated by the fact that the shape of NCs is defined by their growth along certain crystallographic directions and, therefore, the optical axes have a defined (in-plane or out-of-plane) orientation in respect to NCs, the investigation of anisotropic surface plasmon polaritons and hyperbolic surface modes[56] might become possible. More complex stucking of NCs will also allow to study and develop applications of bulk hyperbolic modes, important for super-resolution imaging.[57]

The plasmonic resonances of CuS NCs can be tuned *via* the control of the geometrical parameters (shape and size) in the 800-1600 nm spectral range. This ideally places CuS as an alternative plasmonic material between traditional metals and transition metal nitrides[58] operating in visible and conducting oxides operating above 1500 nm wavelength.[59] In addition to dominant LSPs in the near-infrared spectral range, the CuS nanocrystals also support LSP at shorter wavelengths for out-of-plane polarized light, so that plasmonic properties can be exploited with the same NCs in a very broad spectral range. Additionally, the absorption loss in CuS near the frequency of the plasmonic resonances is lower than in conventional plasmonic materials. The field enhancement and confinement associated with the CuS NCs plasmonic resonances can be used to increase nonlinear phenomena such as second-harmonic generation[60] and optical Kerr-

nonlinearity,[61] enhanced Purcell effect, hot electron generation and associated with it photocalalysis,[62] as well as in sensing applications, which can be engineered in a broad spectral range.

We show that in CuS nanocrystals the width of the Q-factor of the plasmonic mode increases with decreasing refractive index of the surrounding medium due to the anisotropy of the NCs, the trend opposite to that of isotropic plasmonic materials. The LSP resonances in CuS nanocrystals are also tuneable with the NC shape, size and surroundings, offering significant and controllable field enhancement. The measured averaged refractive index sensitivity in the infrared spectral range is approximately 330 nm/RIU which compares favorably with the sensitivity of the LSPs of Au nanoparticles in the visible spectral range and TiN, AZO, ITO nanoparticles in the near infrared.

MATERIALS AND METHODS

Synthesis of CuS nanocrystals.

All chemicals were used as purchased without further purification. Oleylamine (70% OLAM), 1-octadecene (90% ODE), octylamine (99%), hexadecylamine (90%), oleic acid (90% OLAC), sulfur (99.98%), hexane (95%), tertrachloroethylene (anhydrous 99% TCE), chloroform (anhydrous 99%), 1,2-dichlorobenzene (99%) were purchased from Sigma-Aldrich; copper (I) chloride (99.9%) was purchased from Acros Organics; methanol and acetone (HPLC grade) were purchased from Fisher Scientific. All syntheses were carried out in a three-neck flask connected to a Schlenk line under nitrogen atmosphere.

CuS nanocrystals were synthesized according to the following procedure. In a typical synthesis 0.5 mmol CuCl, 6 mmol oleylamine (or a mixture of amines with different C chain length), 1 mmol oleic acid, and 10 mL octadecene were loaded in a three-neck flask and degassed under vacuum at 100°C for 20 minutes. The solution was then purged under nitrogen and heated to 180°C. Once the temperature was stabilized the S-oleylamine solution, obtained by dissolving 2 mmol S in 2 mL oleylamine under nitrogen flow, was injected rapidly. The reaction was allowed to proceed for 3 to 10 minutes and then quenched by cooling down. The NCs were precipitated in methanol by centrifugation and re-dispersed in chloroform, the procedure repeated three times. The final colloid was stored in chloroform under an inert atmosphere. This general procedure produced CuS NCs of 19 nm lateral size, while NCs with smaller aspect ratio, *i.e.* 12 and 16 nm lateral size, were obtained by increasing the amount of oleic acid co-surfactant to 6 and 12 mmol, respectively. NCs with lateral size of 24 nm were obtained by using a mixture of hexadecylamine and oleylamine 1:1. CuS NCs with a lateral size of > 50 nm were synthesized at lower temperatures of 140°C and by the 'inverse' injection of Cu into an S precursor, allowing for a high S concentration to be kept throughout all the synthesis, a pre-requisite to grow CuS in the covellite phase. For this synthesis, 0.5 mmol CuCl, 3 mmol OLAM, 3 mmol octylamine, 1 mmol OLAC were dissolved in 5 mL ODE and degassed at low pressure for 20 min, this solution was successively drop-wise injected (0.5 mL/min) into a previously degassed S/OLAM/ODE precursor, under N_2 atmosphere, at 140°C. The colloidal solution was then washed three times with $CHCl_3$/methanol by centrifuging at 3000 rpm for 5 minutes; this procedure allowed for size-selective precipitation, as the slightly colored supernatant was discarded to eliminate smaller NCs eventually formed as a byproduct.

X-ray diffraction patterns of the NCs with similar thickness and different lateral sizes are in good agreement with the typical diffraction pattern of bulk covellite (Figure S4). For smaller NC sizes, an increase in the (110) signal intensity is observed with increasing the NC lateral size, confirming the preferential growth of CuS NCs in this direction perpendicular to the c axis. On the other hand, by increasing the NC size considerably to more than 50 nm, the intensity of the (110) peak does not increase further, the ratio between the (110) and the (102) peak does not change significantly, while the signal due to overlapping of the (103) and (006) contributions increases considerably. This effect could be due to the fact that such NCs with high aspect ratio have a pronounced tendency to self-assemble into stacks upon solvent evaporation. The preferential orientation of several NCs in the c direction could be responsible for the enhancement of the diffraction pattern in these specific crystallographic orientations.

Characterization techniques.

Transmission electron microscopy images were acquired on a Hitachi 7100 TEM with a filament electron source at 100 kV and with a FEI Tecnai T12. Image analysis was performed with ImageJ software. High resolution TEM micrographs were acquired with a Jeol 2100F STEM at 200kV. The images were processed with ImageJ and Gatan.

Inductively coupled plasma/ Mass Spectrometry (ICP/MS) analyses were carried out with a Perkin Elmer NexION 350D ICP mass spectrometer to determine the concentrations of each element present. The parameters are set as follows: sample flow 0.2 mL/min, gas flow 0.94 mL/min, main plasma gas flow 18 mL/min, auxiliary gas flow 1.2 mL/min and dwell time 100 ms. SO_2 and Cu were measured in a DRC mode (oxygen flow 0.6 mL/min). The composition of CuS NCs was determined by ICP/MS of several samples with different aspect ratio, giving a Cu:S ratio

of 1:1 with a 10% standard deviation (*i.e.*, Cu:S values between 0.89 and 1.1), which is in agreement with the experimental error for S, for which the instrument has a lower sensitivity.

Optical absorption spectra were recorded at room temperature with a UV Solutions U-4100 spectrophotometer. For the size-dependent measurements, colloidal solutions of different samples and with the same NC concentration were prepared, $CHCl_3$ was allowed to evaporate and the colloidal solution was finally dispersed in TCE. For each sample the Cu/S concentration was determined by ICP-MS; this was normalized to the number of atoms contained in each NC, which was determined by the TEM size statistics measurements, knowing the covellite elemental cell parameters.

Theoretical *ab initio* calculations of CuS optical properties.

The energy band structure of CuS in the ideal covellite phase was calculated with the Quasiparticle self-consistent GW (QS*GW*) approximation. The covellite structure has 12 atoms/cell: the Cu and S atoms each split into two classes of 2 and 4 atoms each, respectively. The unit cell is hexagonal, consisting of alternating layers of CuS and Cu-S_2-Cu. Room temperature lattice constants and internal displacement parameters a=3.78813 Å, c=16.33307 Å, u=0.10737 and v=0.06329 were taken from Ref. [18]. As a check, the total energy and forces were calculated with density-functional theory (DFT), using a local density approximation LDA, Perdew-Burke-Ernzerhof PBE and for solids PBEsol functionals. The calculated equilibrium structure was similar in all three cases, and also similar to the measured data,[18] with the main difference that the bond between pairs of equivalent S atoms on the z axis is calculated to be about 2% longer than the measured value.

Through quasiparticle self-consistency (QSGW) one determines the noninteracting Green's function (G0) which is minimally distant from the true Green's function *G*.[40,41] QS*GW* is perhaps

the most universally applicable, true *ab initio* theory for electronic states in extended systems that exists today. It has a proven ability to consistently and reliably predict quasiparticle (QP) levels for a wide range of materials such as graphene,[42] Fe-based superconductors,[43] pyrite,[44] and $NH_3CH_3PbI_3$[45] in a consistent and parameter-free manner that cannot be achieved by other theories. Many other properties, such as Dresselhaus coefficients,[46] electric field gradients,[47] transmission probability,[48] spin waves[50] can also be modelled. The dielectric response of many materials[40] are also in good agreement, though there is a systematic blue shift in plasmon frequencies in insulators because ladder diagrams are left out. Discrepancies with experiment are highly systematic. Another key property of QS*GW* is that, at self-consistency, the poles of $G_0(k; \omega)$ coincide with the peaks in $G(k; \omega)$. Thus, in contrast to density-functional approaches the QS*GW* energy band structure has physical meaning.

Modelling of optical response of CuS nanocrystals.

For this study all the scattering calculations were performed with the discrete dipole approximation (DDA) method. The DDA approach enables accurate modeling of electromagnetic scattering cross sections and near-field calculations of isolated particles of any arbitrary shape, by solving Maxwell's equations through the replacement of a discretized solid particle by an arrangement of N dipoles with a spacing small compared to the wavelength of the incident light.[55] It is assumed that the CuS nanoparticles do not interact with each other; i.e. independent scattering is assumed.

ASSOCIATED CONTENT

Supporting Information

The Supporting Information is available free of charge on the ACS Publications website. Components of the CuS permittivity tensor with and without local field corrections (Figure S1). Isofrequency curves for elliptic, hyperbolic and anisotropic plasmonic dispersion at different wavelengths (Figure S2). TEM and X-ray characterization of CuS NCs (Figure S3). Calculated

absorption cross-sections for diferent in- and out-of-plane illumination for triangular and hexagonal CuS NCs and hexagonal Au, AZO, and ITO nanoparticles (Figure S4). Fitting approach based on the Drude-Sommerfeld model and comparison of the experimental absorption spectra curves for CuS NCs and calculations using dielectric function from *ab initio* calculations and Drude-based approach (PDF).

AUTHOR INFORMATION

Corresponding Author

*E-mail: margoth.cordova_castro@kcl.ac.uk.

Author Contributions

‡These authors contributed equally.

Notes

The authors declare no competing financial interest.

Acknowledgment: This work was supported by the EPSRC project EP/M013812/1. RMCC acknowledges the Mexican National Council of Science and Technology (CONACYT) for doctoral fellowship. ICP/MS metal analysis was performed at the London Metallomics Facility funded by the Welcome trust. We thank the UK Materials and Molecular Modelling Hub for computational resources, which is partially funded by EPSRC (EP/P020194/1). Data access statement: All the data supporting this research are presented in the article and in the supplementary material.

REFERENCES

1. Poddubny, A.; Iorsh, I.; Kivshar, Y.; Hyperbolic Metamaterials. *Nat. Photonics* **2013**, *7*, 958-967.
2. Narimanov, E. E.; Kildishev, A. V. Naturally Hyperbolic. *Nat. Photonics* **2015**, *9*, 214-216.
3. Korzed, K.; Gajc, M.; Pawlak D. A. Compendium of Natural Hyperbolic Materials, *Opt. Exp*. **2015**, *23*, 25406.

4. Drachev V. P., Podolskiy V. A., Kildishev A. V. Hyperbolic Metamaterials: New Physics Behind a Classical Problem, *Opt. Exp*. **2013**, *21*, 15048.
5. Ginzburg, P.; Roth, D. J.; Nasir, M. E.; Segovia, P.; Krasavin, A. V.; Levitt, J.; Hirvonen, L. M.; Wells, B.; Suhling, K.; Richards, D.; Podolskiy, V. A.; Zayats, A. V. Spontaneous Emission in Non-Local Materials. *Light: Science & Applications* **2017**, *6*, e16273.
6. Slobozhanyuk, A.P.; Ginzburg, P.; Powell, D.A.; Iorsh, I.; shalin, A.S.; Segovia, P.; Krasavin, A. V.; Wurtz, G. A.; Podolskiy, V. A.; Belov, P.A.; Zayats, A. V. Purcell Effect in Hyperbolic Metamaterials Resonators. *Phys. Rev. B* **2015**, *92*, 195127.
7. Khurgin, J.B. Replacing Noble Metals With Alternative Materials in Plasmonics and Metamaterials: How Good an Idea?. *Phil. Trans. R. Roc. A* **2016**, *375*, 20160068.
8. Hsieh, W. T.; Wu, P. C.; Khurgin, J. B.; Tsai, D. P.; Liu N.; Sun, G. Comparative Analysis of Metals and Alternative Infrared Plasmonic Materials. *ACS Photonics* **2018**, *5*, 2541-2548.
9. Esslinger, M.; Vogelgesang, R.; Talebi, N.; Khunsin, W.; Gehting, P.; de Zuani, S. Gompf, B.; Kern, Klaus. Tetradymites as Natural Hyperbolic Materials for the Near-Infrared to Visible. *ACS Photonics* **2014**, *1*, 1285-1289.
10. Córdova-Castro, R. M.; Krasavin A. V.; Nasir, M. E.; Zayats, A. V.; Dickson, W. Nanocone-based Plasmonic Metamaterials, *Nanotechnology* **2019**, *30*, 055301.
11. Coronado, E. A.; Shatz, G. C. Surface Plasmon Broadening for Arbitrary Shape Nanoparticles: A Geometrical Probability Approach. *J. Chem. Phys.* **2003**, *119*, 3926-3934.

12. Kelly, K. L.; Coronado, E.; Zhao, L. L.; Schatz, G. C. The Optical Properties of Metal Nanoparticles: The influence of Size, Shape, and Dielectric Environment. *J. Phys. Chem. B* **2003**, *107*, 668-677.

13. Mayer, K. M.; Hafner, J. H. Localized Surface Plasmon Resonance Sensors. *Chem. Rev.* **2011**, *11*, 3828-2857.

14. Wang, P.; Krasavin, A. V.; Viscomi, F. N.; Adawi, A. M.; Bouillard, J-S G.; Zhang, L.; Roth, D. J.; Tong, L.; Zayats, A. V. Metaparticles: Dressing Nano-Objects with a Hyperbolic Coating. *Laser Photonics Rev.* **2018**, *12*, 1800179.

15. Van der Stam, W.; Akkerman, Q. A.; Ke, X.; van Huis, M. A.; Bals, S.; de Mello Donega, C. Solution-Processable Ultrathin Size- and Shape-Controlled Colloidal Cu2−xS Nanosheets. *Chem. Mater.* **2015**, *27*, 283−291.

16. Saldanha, P. L.; Brescia, R.; Prato, Mirko.; Li, H.; Povia, M.; Manna, L.; Lesnyak, V. Generalized One-Pot Synthesis of Copper Sulfide, Selenide-Sulfide, and Telluride-Sulfide Nanoparticles. *Chem. Mater.* **2014**, *26*, 1442−1449.

17. Xie, Y.; Carbone, L.; Nobile C.; Grillo V.; D'Agostino S.; Sala F. D.; Giannini, C.; Altamura, D.; Oelsner C.; Kryschi, C.; Cozzoli, P. D. Metallic-like Stoichiometric Copper Sulfide Nanocrystals: Phase- and Shape-Selective Synthesis, Near-Infrared Surface Plasmon Resonance Properties, and Their Modeling. *ACS Nano* **2013**, *7*, 7352–7369.

18. Gotsis, H. J., Barnest, A. C. and Strange, P. *J. Phys.: Cond. Matt.* **1997**, *4* 10461-10468.

19. Page, M.; Niitsoo, O.; Itzhaik, Y.; Cahen, D. and Hodes, G. Copper Sulfide as a Light Absorber in Wet-Chemical Synthesized Extremely Thin Absorber (ETA) Solar Cells. *Energy and Environmental Sci.* **2009**, *2*, 220-223.

20. Wu, Y.; Wadia, C.; Ma, W. L.; Sadtler, B.; Alivisatos, A. P. Synthesis and Photovoltaic Application of Copper (I) Sulfide Nanocrystals. *Nano Lett.* **2008**, *8*, 2551-2555.

21. Basu, M.; Sinha, A.K.; Pradhan, M.; Sarkar, S.; Negishi, Y.; Govind; Pal, T. Evolution of Hierarchical Hexagonal Stacked Plates of CuS from Liquid-Liquid Interface and its Photocatalytic Application for Oxidative Degradation of Different Dyes under Indoor Lighting. *Environ. Sci. Technol.* **2010,** *44*, 6313–6318.

22. De, B.; Balamurugan, J.; Kim, N. H.; Lee, J. H. Enhanced Electrochemical and Photocatalytic Performance of Core−Shell CuS@Carbon Quantum Dots@Carbon Hollow Nanospheres. *ACS Appl. Mater. Interfaces* **2017**, *9*, 2459−2468.

23. Xie, Y.; Bertoni, G.; Riedinger A.; Sathya, A.; Prato, M.; Marras, S.; Tu, R.; Pellegrino, T.; Manna, L. Nanoscale Transformations in Covellite (CuS) Nanocrystals in the Presence of Divalent Metal Cations in a Mild Reducing Environment. *Chem. Mater.* **2015**, *27*, 7531−7537.

24. Wang, S.; Riedinger, A.; Li, H.; Fu, CH.; Liu, H.; Li, L.; Liu, T.; Tan, L.; Barthel, M. J.; Pugliese, G.; De Donato, F.; D'Abbusco, M. S.; Meng, X.; Manna, L.; Meng, H.; Pellegrino, T. Plasmonic Copper Sulfide Nanocrystals Exhibiting Near-Infrared Photothermal and Photodynamic Therapeutic Effects. *ACS Nano* **2015**, *9*, 1788-1800.

25. Marin B. C.; Hsu S.-W.; Chen L.; Lo A.; Zwissler D. W.; Liu Z.; Tao A. R. Plasmon-Enhanced Two-Photon Absorption in Photoluminiescent Semiconductor Nanocrystals. *ACS Photonics* **2016**, *3*, 526-531.

26. Kriegel, I.; Jiang, C.; Rodriguez-Fernandez, J.; Schallarsi, R.D.; Talapin, D. V.; da Como, E.; Feldmann, J. Tuning the Excitonic and Plasmonic Properties of Copper Chalcogenide Nanocrystals *J. Am. Chem. Soc.* **2012**, *134*, 1583−1590.

27. Luther, J. M.; Jain P. K.; Ewers, T.; Aliviasatos, A. P. Localized Surface Plasmon Resonances Arising From Free Carriers in Doped Quantum Dots. *Nat. Mater.* **2011**, *10*, 271.

28. Xie Y.; Chen W.; Bertoni G.; Kriegel I.; Xiong M.; Li N.; Prato M.; Riedinger A.; Sathya A.; Manna L. Tuning and Locking the Localized Surface Plasmon Resonances of CuS (Covellite) Nanocrystals by an Amorphous $CuPd_xS$ Shell. *Chem. Mater* **2017**, *29*, 1716-1723.

29. Kalanur S. S.; Seo H. Tuning Plasmonic Properties of CuS Thin Films *Via* Valence Band Filling. *RSC Adv.* **2017**, *7*, 11118-11122.

30. Hsu, S.-W.; Ngo, C.; Tao, A. R. Tunable and Directional Plasmonic Coupling within Semiconductor Nanodisk Assemblies. *Nano Lett.* **2014**, *14*, 2372-2380.

31. Hsu,S.-W.; On, K.; Tao, A. R. Localized Surface Plasmon Resonances of Anisotropic Semiconductor Nanocrystals. *J. Am. Chem. Soc.* **2011**, *133*, 19072-19075.

32. Guan, J.; Peng, J.; Jin, X. Synthesis of Copper Sulfide Nanorods as Peroxidase Mimics for the Colorimetric Detection of Hydrogen Peroxide. *Anal. Methods* **2015**, *7*, 5454-5461.

33. Comin, A.; Manna, L. New Materials for Tunable Plasmonic Colloidal Nanocrystals. *Chem. Soc. Rev.* **2014**, *43*, 3957-3975.

34. Hsu S.W.; Ngo Ch.; Bryks W.; Tao A. R. Shape Focusing During the Anisotropic Growth of CuS Triangular Nanoprisms. *Chem. Mater.* **2015**, *27*, 4957-4963.

35. Gaspari, R.; Manna, L.; Cavalli, A. A Theoretical Investigation of the (0001) Covellite Surfaces. *J. Chem. Phys.* **2014,** *141*, 044702.

36. Guo, Q.; Yao, Y.; Luo, Z-C.; Qin, Z.; Xie, G.; Liu, M.; Kang, J.; Zhang, S.; Bi, G.; Liu, X.; Qiu, J. Universal Near-Infrared and Mind-Infrared Optical Modulation for Ultrafast

Pulse Generation Enable by Colloidal Plasmonic Semiconductor Nanocrystals. *ACS Nano* **2016**, *10*, 9463-9469.

37. Lei H.; Huining L.; Fang Y.; Derong C. Transparent Heat Insulation Coating With High Selective Shielding Ability Designed With Novel Superstructures of Copper Sulfide Nanoplates. *J Mater Sci*. **2019**, *54*, 302-312.
38. Maixian, L.; Xiaozheng X.; Chayanjit G.; Xin L.; Yang L.; Edward P. F.; Mark T. S.; Paras N. P. Room-Temperature Synthesis of Covellite Nanoplates with Broadly Tunable Localized Sirface Plasmon Resonance. *Chem. Mater.* **2015**, *27*, 2584-2590.
39. Gotsis, H. J.; Barnes, A. C.; Strange, P. Experimental and Theoretical Investigation of the Crystal Structure of CuS. *J. Phys.: Condens. Matter* **1992**, *4*, 10461.
40. Kotani, T.; van Schilfgaarde, M.; Faleev, S. V. Quasiparticle Self-Consistent GW Method: A Basis for the Independent-Particle Approximation. *Phys. Rev. B* **2007**, *76*, 165106.
41. Ismail-Beigi, S. Justifying Quasiparticle Self-Consistent Schemes *via* Gradient Optimization in Baym–Kadanoff Theory. *J. Phys.: Condens. Matter* **2017**, *29*, 385501
42. van Schilfgaarde, M.; Katsnelson, M. I. First-Principles Theory of Nonlocal Screening in Graphene. *Phys. Rev. B* **2011**, *83*, 081409.
43. Tomczak, J. M.; van Schilfgaarde, M.; Kotliar, G. Many-Body Effects in Iron Pnictides and Chalcogenides: Nonlocal *Versus* Dynamic Origin of Effective Masses. *Phys. Rev. Lett.* **2012**, *109*, 237010.
44. Lehner, S. W.; Newman, N.; Bandyopadhyay, S.; van Schilfgaarde, M.; Savage, K.; Buseck, P. R. Defect Energy Levels and Electronic Behavior of Ni-, Co-, and As-Doped Synthetic Pyrite (FeS_2) *J. Appl. Phys.* **2012**, *111*, 083717.

45. Azarhoosh, P.; McKechnie, S.; Frost, J. M.; Walsh, A.; van Schilfgaarde, M.; Research Update: Relativistic Origin of Slow Electron Hole Recombination in Hybrid Halide Perovskite Solar Cells. *APL Mater.* **2016**, *4*, 091501.

46. Chantis, A. N.; van Schilfgaarde, M.; Kotani, T. *Ab Initio* Prediction of Conduction Band Spin Splitting in Zinc Blende Semiconductors, *Phys. Rev. Lett.* **2006**, *96*, 086405.

47. Christensen, N. E.; Svane, A.; Laskowski, R.; Palanivel, B.; Modak, P.; Chantis, A. N.; van Schilfgaarde, M.; Kotani, T. Electronic Properties of 3R-$CuAlO_2$ under Pressure: Three Theoretical Approaches. *Phys. Rev. B* **2010**, *81*, 045203.

48. Faleev, S. V.; Mryasov, O. N.; van Schilfgaarde, M. Effect of Correlations on Electronic Structure and Transport across (001) Fe/MgO/Fe Junctions. *Phys. Rev. B* **2012**, *85*, 174433.

49. Kotani T.; van Schilfgaarde, M. Spin Wave Dispersion Based on the Quasiparticle Self-Consistent GW Method: NiO, MnO and α-MnAs. *J. Phys.: Condens. Matter* **2008**, *20*, 295214.

50. Lukashev, P.; Lambrecht, W. R.; Kotani, T.; van Schilfgaarde, M. Electronic and Crystal Structure of $Cu_{2-x}S$: Full-Potential Electronic Structure Calculations. *Phys. Rev. B* **2007**, *76*, 195202.

51. Bruneval, F.; Vast, N.; Reining, L.; Izquierdo, M.; Sirotti, F.; Barrett, N. Exchange and Correlation Effects in Electric Excitations of Cu_2O. *Phys. Rev. Lett.* **2006**, *97*, 267601.

52. Handbook of Optical Constants of Solids; Palik, E. D., Ed.; Academic Press: San Diego, **1998**.

53. Chen, H.; Kou, X.; Yang, Zhi.; Ni, W.; Wang, J. Shape- and Size-Dependent Refractive Index Sensitivity of Gold Nanoparticles. *Langmuir* **2008**, *24*, 5233-5237.

54. Vasilantonakis, N.; Wurtz, G. A.; Podolskiy, V. A.; Zayats, A. V. "Refractive Index Sensing with Hyperbolic Metamaterials: Strategies for Biosensing and Nonlinearity Enhancement," *Opt. Exp*. **2015**, *23*, 14329-14343.

55. Draine, B. T.; Flatau, P. J. Discrete-Dipole Approximation for Scattering Calculations. *J. Opt. Soc. Am. A* **1994**, *11*, 1491-1499.

56. High, A. A.; Devlin, R. C.; Dibos, A.; Polking, M.; Wild, D. S.; Perczel, J.; de Leon, N. P.; Lukin, M. D.; Park, H. Visible-frequency Hyperbolic Metasurface. Nature **2015**, *522*, 192-196.

57. Liu, Z. W.; Lee, H. ; Xiong, Y.; Sun, C.; Zhang, X. Far-field Optical Hyperlens Magnifying Sub-diffraction-limited Objects. Science **2007**, *315*, 1686-1686.

58. Guler, U.; Boltasseva, A.; Shalaev, V. M. Refractory Plasmonics, Science **2007**, *344*, 263-264.

59. Naik, G. V.; Shalaev, V. M.; Boltasseva, A. Alternative Plasmonic Materials: Beyond Gold and Silver, Adv. Mater. **2013**, *25*, 3264-3294.

60. Wells, B.; Bykov, A. Y.; Marino, G.; Nasir, M. E.; Zayats, A. V.; Podolskiy, V. A. Structural Second-order Nonlinearity in Plasmonic Metamaterials. Optica **2018**, *5*, 1502-1507.

61. Neira, A. D.; Olivier, N.; Nasir, M. E.; Dickson, W.; Wurtz, G. A.; Zayats, A. V. Eliminating Material Constraints for Nonlinearity with Plasmonic Metamaterials. Nat. Commun. **2015**, *6*, 7757.

62. Naldoni, A.; Shalaev, V. M.; Brongersma, M. L. Applying Plasmonics to a Sustainable Future. Science **2017**, *356*, 908-909.

Supporting Information

Anisotropic Plasmonic CuS Nanocrystals as Natural Electronic Material with Hyperbolic Optical Dispersion

R. Margoth Córdova-Castro[‡], Marianna Casavola[‡], Mark van Schilfgaarde, Alexey V. Krasavin, Mark Green, David Richards, and Anatoly V. Zayats*

Department of Physics and London Centre for Nanotechnology, King's College London, London WC2R 2LS, United Kingdom

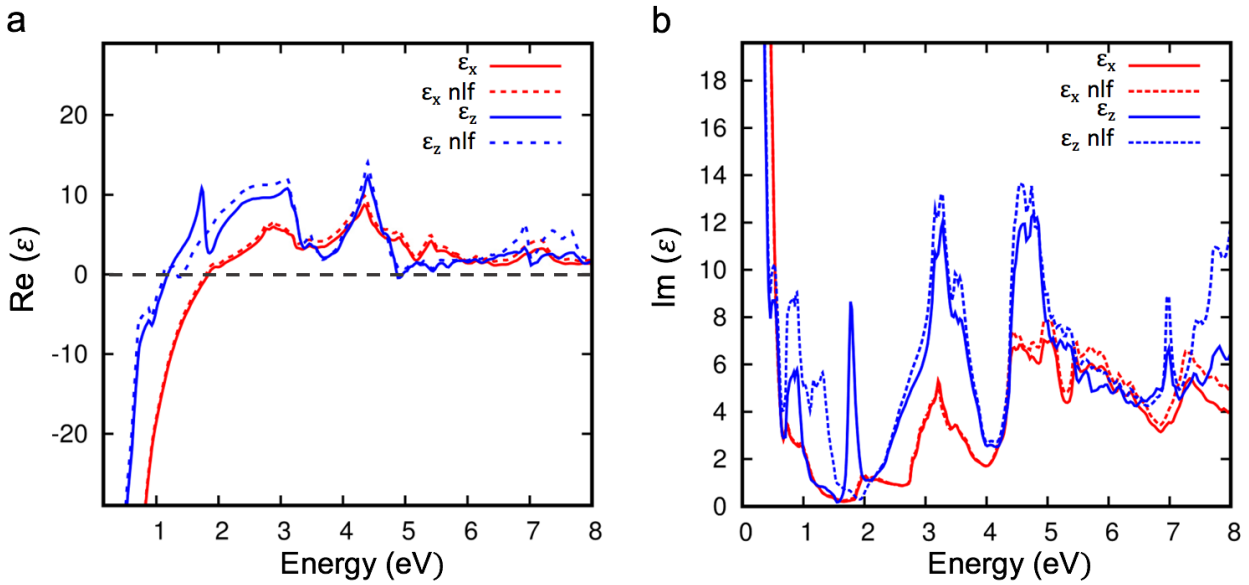

Figure S1. Longitudinal components $\varepsilon_x=\varepsilon_y$ and ε_z of the (a) real and (b) imaginary parts of the dielectric function, with (dashed lines) and without (solid lines) local field corrections.

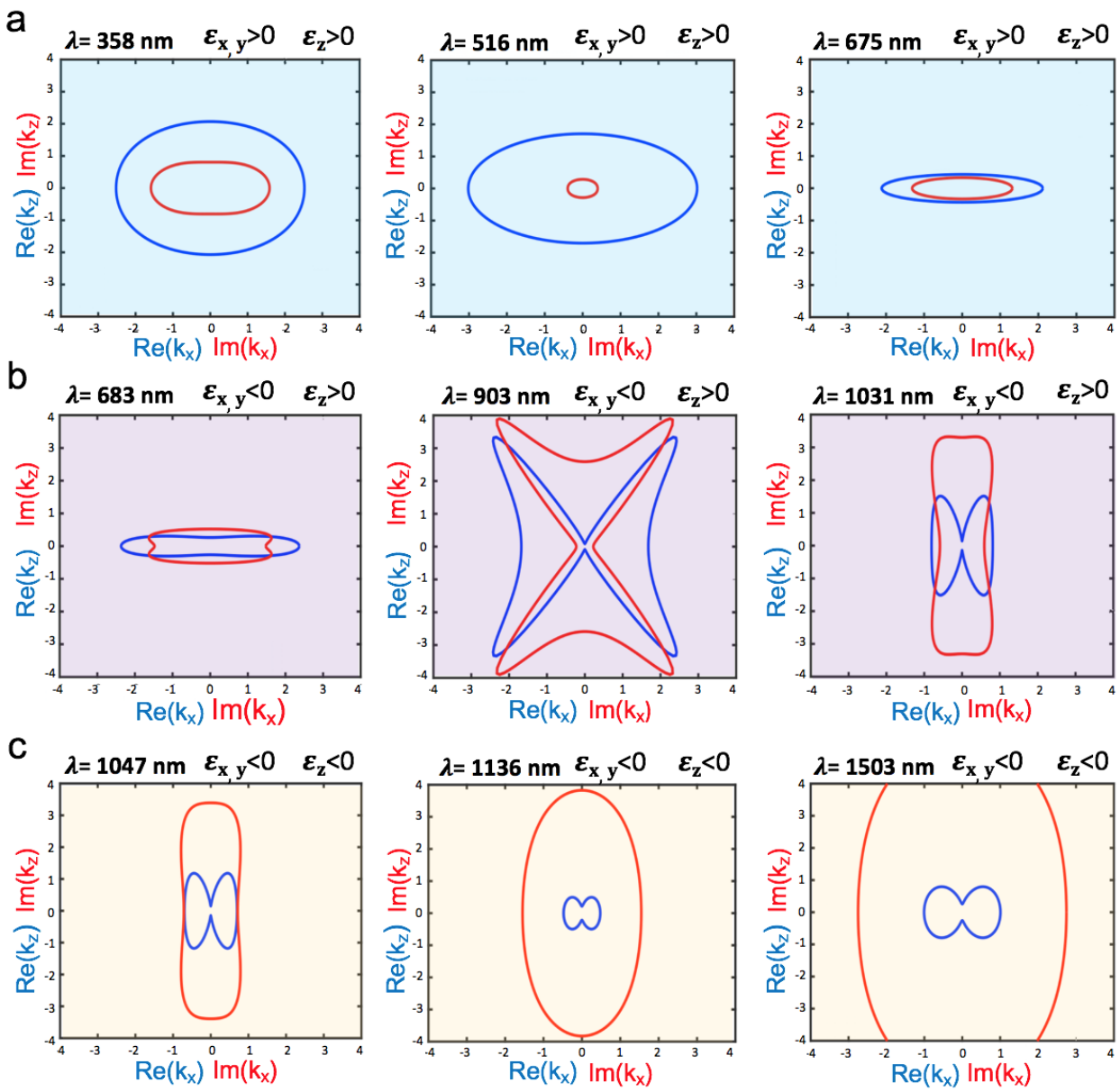

Figure S2. Isofrequency curves for (blue) [Re{$k_x(\omega)$},Re{$k_y(\omega)$}=0, Re{$k_z(\omega)$}], refractive index related, and (red) [Im{$k_x(\omega)$}, Im{$k_y(\omega)$}=0, Im{$k_z(\omega)$}], absorption related, parts of the wavevector wavevector for the TM electromagnetic waves with the electric field component in z-direction in bulk anisotropic CuS for the vacuum wavelengths $\lambda = 2\pi/\omega$ in different dispersion regimes: (c) elliptic (anisotropic dielectric), (d) hyperbolic and (e) anisotropic plasmonic.

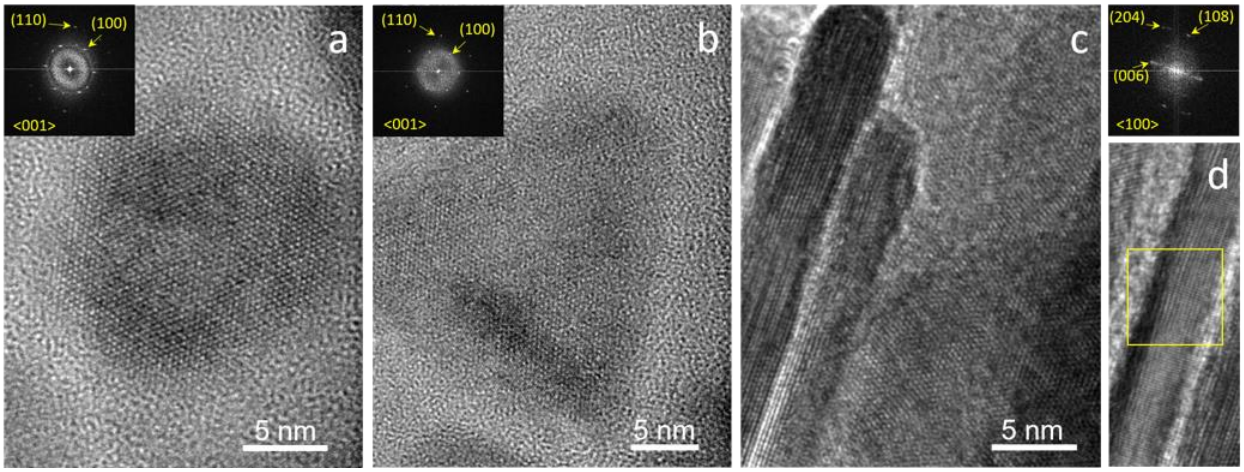

Figure S3. (a-c) HRTEM micrograph of (a) a CuS NC of a 16 nm lateral size with a circular shape in the <001> zone axis; (b) a CuS NC of a 24 nm lateral size with quasi-triangular shape in the <001> zone axis, (c-d) CuS NCs of a 127 nm lateral size lying flat (a,b) and vertically oriented (c,d) on the substrate. The insets show the fast Fourier transform (FFT) of the corresponding micrographs.

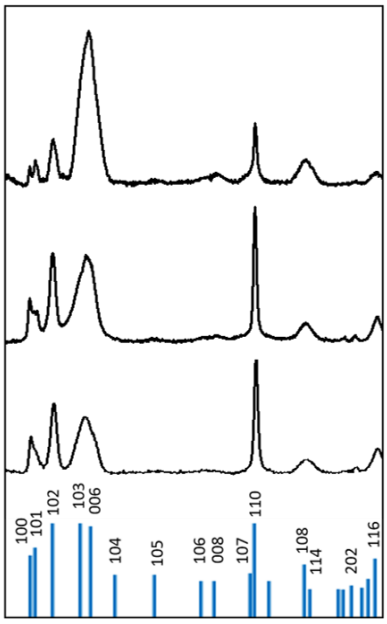

Figure S4. X-Ray Diffraction (XRD) patterns of CuS NCs of (from bottom to top) 16, 24, and a 56 nm lateral size. For comparison a standard XRD pattern of covellite CuS (reference: CuS #01-075-2233) is plotted in blue.

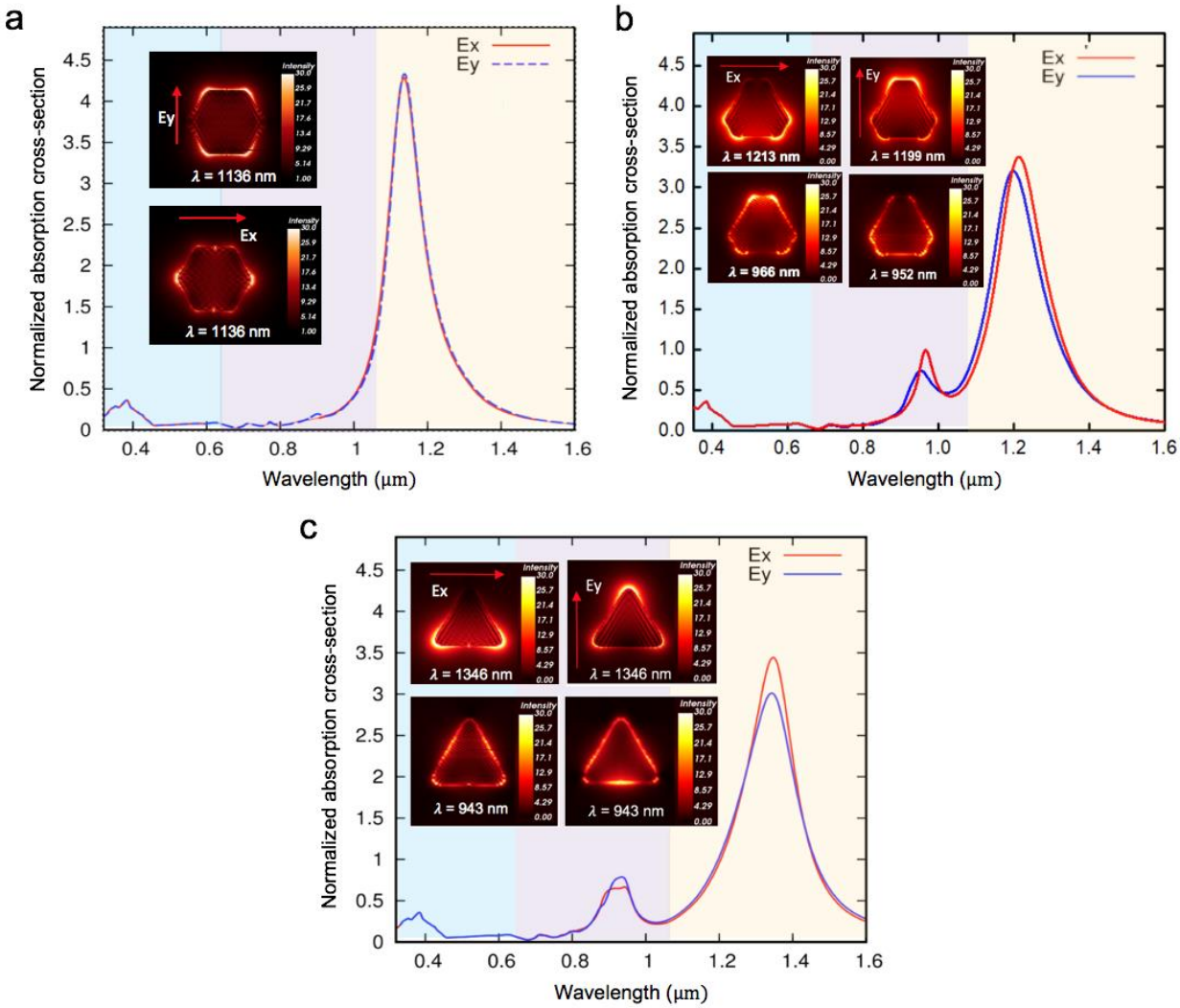

Figure S5. Calculated spectra of normalized absorption cross-sections for (a) hexagonal (b) hexa-triangular and (c) a triangular shape (upon illumination with a linearly polarized plane wave with the electric field along *x* and the *z* axis, respectively. Near field intensity maps are shown at the corresponding resonant wavelengths for each direction.

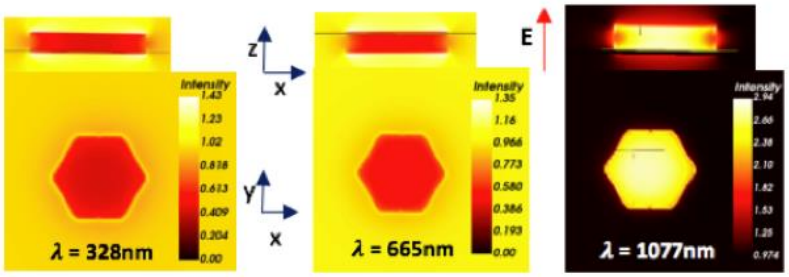

Figure S6. Near field intensity maps for the CuS NC of a hexagonal shape of a 19 nm lateral size and a 5 nm thickness surrounded by a medium with a refractive index of 1.45, calculated at the spectral absorption peaks (Fig. 4b) for out-of-plane polarized illumination.

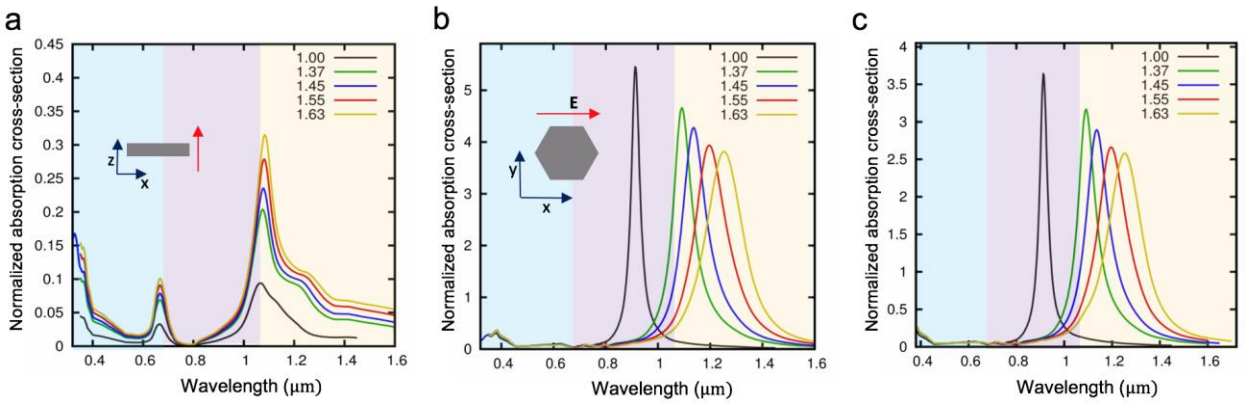

Figure S7. Calculated spectra of normalized absorption cross-sections for CuS isolated nanocrystals of a hexagonal shape surrounded by various dielectric media and illuminated with a linearly polarized plane wave with the electric field along (a) *z* axis (b) *x* axis and c) average of the field along *x*, *y*, and *z* axes with the corresponding anisotropic dielectric function for each axis.

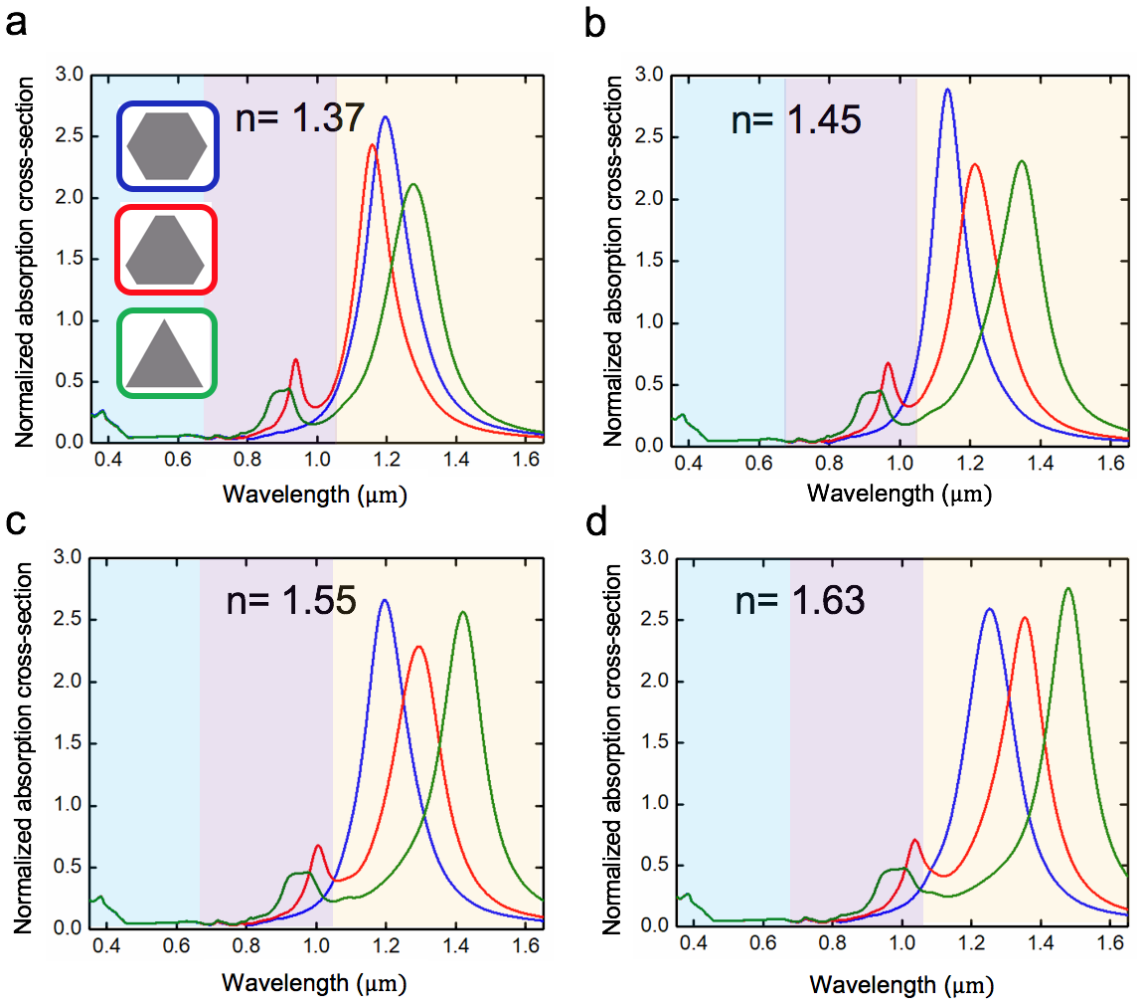

Figure S8. Calculated spectra of normalized absorption cross-sections for CuS nanocrystals of a hexagonal, triangular and hexa-triangular shapes (19 nm lateral size and 5 nm thickness) surrounded by a medium with different refractive inexes as indicated in the panels. The spectra are averaged over random NC orientations with respect to the linearly polarised incident light.

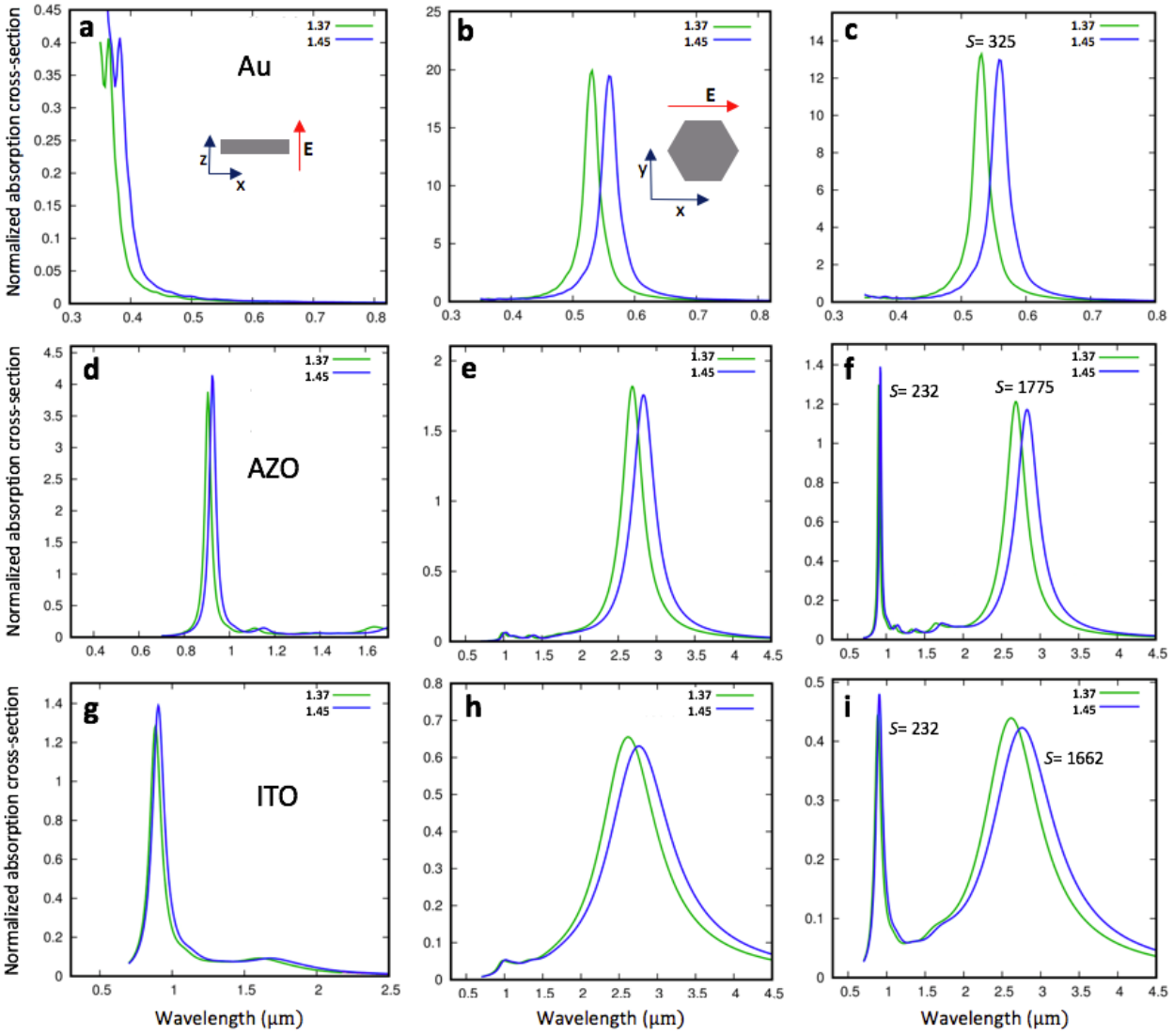

Figure S9. Calculated spectra of normalized absorption cross-sections for hexagonal nanoparticles (19 nm size and 5 nm thickness) dispersed in solvents with refractive indice s of 1.37 and 1.45 for (a-c) Au, (d-f) AZO an (g-i) ITO: (a,d,g) and (b,e,h) light polarization normal and in-plane of the nanoparticles, respectively, (c,f,i) average response of randomly oriented nanoparticles.

Fitting approach based on the Drude-Sommerfeld model.

In previously reported studies,[14,26-30] the complex dielectric function of CuS nanocrystals was calculated using the Drude-Sommerfeld model

$$\varepsilon(\omega) = \varepsilon_\infty - \omega_p/(\omega^2 + i\gamma\omega), \quad (4)$$

where ε_∞ takes into account the polarization background of the ion cores, γ is the damping constant and ω_p is the Drude plasma frequency. These studies solved an inverse problem by taking the experimental values for the width of the resonance absorption curve to determine γ, and the maximum of the absorption peak in the measured absorption spectral curve to determine the frequency of the localized surface plasmon resonance ω_{LSP}. The plasma frequency ω_p (defined by Eq. 4) is then evaluated from the real part of the Drude-Sommerfeld permittivity $\mathrm{Re}\{\varepsilon(\omega_{LSP})\} = 1 - \omega_p^2/({\omega_{LSP}}^2 + \gamma^2)$ and the analytical solution, averaged over nanoparticle orientations, corresponding to the resonant conditions of an oblate spheroid $\mathrm{Re}\{\varepsilon(\omega_{LSP})\} = \varepsilon_m[(L_j - 1)/L_j]$ for *j*=1,2,3, where L_j is the geometrical factor of the spheroid and ε_m is the permittivity of the surrounding medium.

We also follow this approach to show that this procedure will reproduce calculated absorption spectra very similar to the experimental measurements, as expected since the parameters were derived from the experimental curves. Nevertheless, the permittivity derived following this approach is incorrect even if a match with the experimental extinction spectra is obtained. For example, for the experimental extinction curve with $\omega_{LSP} = 1.13$ eV, observed for CuS NCs immersed in a medium of 1.45 refractive index (Figure 4a), and taking into account ε_∞=1 and $\varepsilon_m = 1.8769$ in the analytical solution for the resonant condition of an oblate spheroid with aspect ratio of $h = (a/c) = 3.8$, $L_1 = L_2 = 0.154$ and $L_3 = 1 - 2(L_1) = 0.6921$, we obtain $\omega_p = 4.01$ eV and the damping constant $\gamma = 0.39$ eV. Figure S9 shows the comparison of the absorption visible spectral curve of CuS calculated using the complex dielectric function determined with the Drude-Sommerfield approach and using the complex dielectric function calculated from first principles using QS*GW* and RPA. However, in the latter case the two free fitting parameters, ω_p and γ, must be changed to obtain an agreement for different refractive indices of surroundings and do not correctly describe properties of the material away from the LSP resonance or the polarization properties of individual NCs. In particular, the Drude-Sommerfeld approach does not correctly describe the sensitivity of the CuS LSP resonance on the solvent's

refractive index and the NC size. On the other hand, the use of permittivity evaluated from the *ab initio* band structure allows the correct prediction of the frequency of LSPs, and their refractive index dependences, without any fitting parameters, while the deviations in the width of the resonances is considered to be related to the dispersion of the nanocrystal size. The use of the fitting within the Drude formalism might have been justifiable for a NC made from an isotropic material, but completely breaks down for anisotropic materials such as CuS.

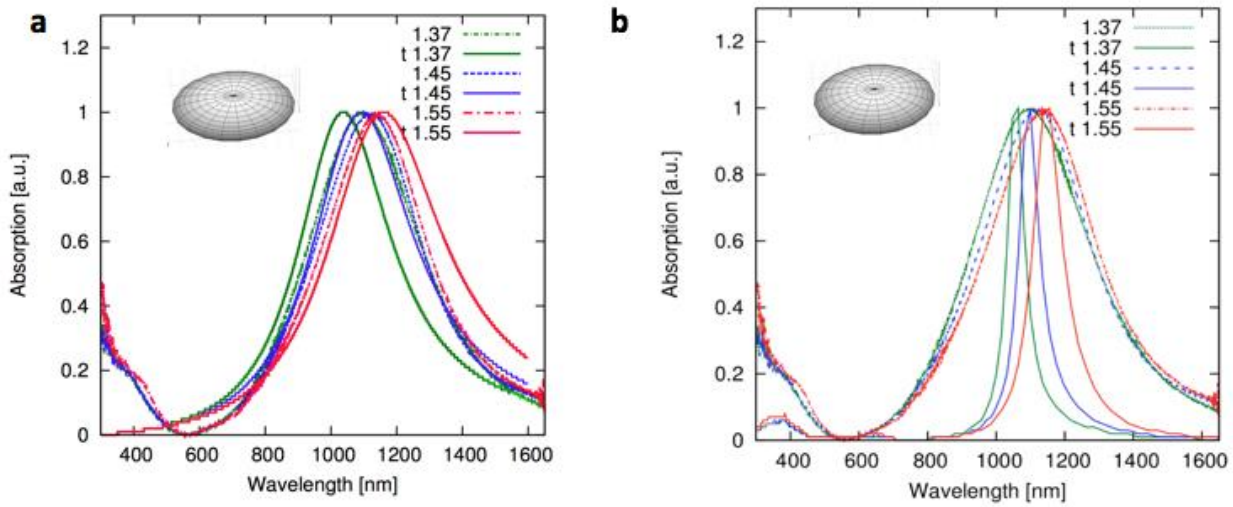

Figure S10. (a) Experimental (dashed/dotted lines) and theoretically fitted (t, solid lines) normalized absorption spectra for an isolated oblate spheroid using the Drude model for the NC permittivity: the plasma frequency and damping coefficient are used as fitting parameters. The refractive indeces of surroundings for different curves are indicated in the legends. (b) Same as (a) but for the anisotropic permittivity obtained from the *ab initio* calculations. A random orientation of the spheroidal particles is assumed in both (a) and (b).